Free-boundary problems for wave-structure interactions in shallow-water: DG-ALE description and local subcell correction

Ali Haidar, Fabien Marche, François Vilar

Free-boundary problems for wave-structure interactions in shallow-water: DG-ALE description and local subcell correction

Ali Haidar · Fabien Marche · François Vilar

Abstract We introduce a robust numerical strategy for the numerical simulation of several free-boundary problems arising in the study of nonlinear wave-structure interactions in shallow-water flows. We investigate two types of boundary-evolution equations: (i) a *kinematic*-type equation, associated with the interaction of waves with a moving lateral wall, (ii) a *fully-nonlinear* singular equation modeling the evolution of the interface between a solid obstacle placed on the surface and the fluid. At the continuous level, the flow is globally modeled with the hyperbolic Nonlinear Shallow-Water (NSW) equations, including varying topography, and at the discrete level, an arbitrary-order discontinuous Galerkin (DG) method is stabilized with a Local Subcell Correction (LSC) method. Mimicking the theoretical study of the continuous problem, suitable diffeomorphisms are introduced to recast the moving-boundary problems into fixed-boundary ones, and to compute the boundary's evolution through an Arbitrary-Lagrangian-Eulerian (ALE) description. For any order of polynomial approximation, the resulting global algorithm is shown to: (i) preserve the Discrete Geometric Conservation Law (DGCL), (ii) ensure the preservation of the water height positivity at the sub-cell level, (iii) preserve the class of motionless steady-states (well-balancing), possibly with the occurrence of a partly immersed obstacle. Several numerical computations highlight that the proposed strategy: (i) effectively approximate the new free-boundary IBVPs introduced in [19], (ii) is able to accurately handle strong flow singularities without any robustness issues, (iii) retains the highly accurate subcell resolution of DG schemes.

Keywords free-boundary · shallow-water · discontinuous Galerkin · local subcell · Arbitrary-Lagrangian-Eulerian · wave-structure interaction

1 Introduction

Fluid-structure interactions generally refer to a wide class of multi-physics problems, involving possibly deformable structures and a surrounding (and/or sometimes internal) fluid. Such problems are inherently difficult to model, partly due to the disparate mathematics and numerics needed to describe the fluid and the structure areas, and the various scales of the underlying physical processes. The mathematical and numerical studies of wave-structure interactions, for instance in the modeling of ship motions, wave-breakers or marine renewable energy devices, also come with their own difficulties, as (at least part of) the boundary of the domain on which the equations are cast may depend on time. Such a boundary's motion may either be enforced or be part of the problem's unknowns, the boundary's spatial location being generally modeled by some evolution equations depending on the current solution of the fluid model.
Concerning the fluid modeling, water-waves and free-surface flows have been intensively studied in recent years, both from theoretical and computational sides (see [23] for a detailed insight into the theory). Using the free-surface Euler equations generally remains unworkable for practical applications and simpler asymptotic models, exploiting the scaling of specific flow regimes, may be used instead. In particular, shallow-water models may benefit from the vertical structure of the velocity field in shallow-water to discard the dependency on the vertical variable. Among shallow-water models, the hyperbolic NSW equations of [9] are one of the most widely used set of equations for simulating long-wave hydrodynamics.

corresponding author: E-mail: ali.haidar@univ-cotedazur.fr

The NSW equations may be conveniently written as follows:

$$\partial_t \mathbf{v} + \partial_x \mathbf{F}(\mathbf{v}, b) = \mathbf{B}(\mathbf{v}, b'), \tag{1}$$

where $\mathbf{v} : \Omega \times \mathbb{R}_+ \ni (x,t) \mapsto \mathbf{v}(x,t) = (\eta, q) \in \Theta$ gathers the flow's conservative variables, $\eta := H + b$ is the free-surface elevation, H the water-height, u is the horizontal (depth-averaged) velocity, $q := Hu$ the horizontal discharge, $b : \mathbb{R} \to \mathbb{R}$ is a smooth function describing the topography (see Fig.1) and the convex and open set Θ is defined as

$$\Theta := \{\mathbf{v} \in \mathbb{R}^2,\ H \geq 0\}, \tag{2}$$

$\mathbf{F} : \Theta \times \mathbb{R} \to \mathbb{R}^2$ is the (nonlinear) flux function and $\mathbf{B} : \Theta \times \mathbb{R} \to \mathbb{R}^2$ is the topography source term, respectively defined as follows:

$$\mathbf{F}(\mathbf{v}, b) := \begin{pmatrix} q \\ uq + \frac{1}{2} g \eta (\eta - 2\, b) \end{pmatrix}, \quad \mathbf{B}(\mathbf{v}, b') := \begin{pmatrix} 0 \\ -g\, \eta\, b' \end{pmatrix}. \tag{3}$$

The benefits of using this pre-balanced formulation (instead of the classical form) are highlighted in [24, 11]. On the theoretical side, the well-posedness of hyperbolic IBVP problems has been widely studied, see for instance [3], and from a numerical viewpoint, numerous studies relying on a large range of methods can be found, see [17] and all the references therein and below. Considering their hydrostatic and hyperbolic nature, in comparison to the dispersive nature of more sophisticated models such as the Boussineq-type models, the NSW equations generally provide an accurate representation of nearshore flows in the surf-zone and steep-fronted surface waves, such as dam-breaks, flood waves or bores.
There are far less studies relying on shallow-water models to study wave-structure interactions. On the numerical side, taking apart the study of one-way interactions of surface-waves with fixed surface-piercing topography (including for instance wave reflexion, run-up, overtopping and submersion), which can be accurately modeled without considering moving or free-boundary problems, see for instance [12,11], we may refer to [13] for the study of congested flows, to the simulation of surface-piercing structures in heaving motions in [5] or to [4] for the study of a toy-model for wave-energy conversion. On the theoretical side, the recent works [6,2] focus on the interactions between waves in the Boussinesq regime and partly immersed objects are investigated. A general theory for a class of quasi-linear hyperbolic IBVPs with a moving and/or free-boundary is introduced in [19] for the horizontal surface dimension $d = 1$, and applied to the NSW equations, inspiring the numerical study proposed in the present work.
From a numerical viewpoint, the study of free-boundary flows is also a difficult problem. To avoid interface-tracking methods, one may require the formulation to handle moving domains in a robust way, while ensuring the needed accuracy and conservation properties. Additionally, the flow interaction with a moving boundary may also result in complex unsteady phenomena, coming with the need of high-order accurate approximations to resolve the unsteadiness at various scales. In such a context, the Arbitrary Lagrangian-Eulerian (ALE) method is a popular choice for flow problems involving time-varying boundaries. Initially developed within some Finite-Difference (FD) methods in [18], and later extended to Finite-Element (FE) and Finite-Volume (FV) methods, see for instance [10] for a review, the ALE method is generally put forward as combining the best of both Lagrangian and Eulerian worlds: the mesh move with an arbitrary velocity, which may be chosen independently from the material velocity. This provides a welcome flexibility, avoiding the explicit tracking of interfaces of purely Eulerian approaches, as well as the large distortions generally encountered in the pure Lagrangian framework for large time evolutions and spatial motions.
Besides the issue of handling moving meshes, reaching an optimal (possibly high-) order of accuracy where the solution is smooth is also a major concern in the design of discrete formulations for such problems and the development of high-order methods for solving real-world problems is a broad and very active research topic in computational physics. In this context, discontinuous Galerkin (DG) methods have encountered considerable improvements in recent years. They are now widely used in several large classes of problems, in fluid dynamics, geophysical flows, aero-acoustics or electro-magnetism. We refer the reader to the review [8] for more details and references concerning the various applications of DG methods to flow problems. It is known that DG methods successfully combine features and capabilities coming from both FE methods and FV methods, accounting for the underlying physical processes. Among the assets of DG methods, let mention the arbitrary-order of accuracy in space, the compact stencils (in comparison with high-order FV methods), the compliance towards complex geometries and general unstructured / non-conforming meshes or h/p-adaptivity. DG methods with an ALE description for moving boundaries

problems in fluid-structure interactions or free-surface flows have also been considered for instance in [31, 25, 26], or in the (closely related) *space-time* DG methods of [30, 29]. Let also mention the recent Residual Distribution (RD) formulation in ALE description for the NSW on the sphere proposed in [1].

In the present work, taking inspiration from [19], we numerically investigate free-boundary one-dimensional hyperbolic problems arising in the study of nonlinear surface-wave/structure interactions. Specifically, considering (1) cast on the bounded moving domain $\Omega_t := (a, \chi(t))$, we aim at designing a robust and accurate DG discrete formulation, with an underlying ALE description which is directly modeled from the class of free-boundary IBVP introduced in [19]. Besides the simpler case of a moving boundary with a prescribed motion, which may be illustrated for instance by the forced motion of a wave-maker paddle in a basin, we consider two important kinds of problems:

♯1 *free-boundary with kinematic-type evolution:* the boundary evolution is obtained as the solution of a nonlinear equation depending on $\mathbf{v}$:

$$\dot{\chi}(t) = \Upsilon(\mathbf{v}_{|\chi}(t)),$$

where Υ is a smooth function. This is illustrated by the interactions of waves with a moving wall, mimicking the response of a piston and modeling a simplified wave-energy convertor [4],

♯2 *free-boundary with fully-nonlinear evolution:* the boundary's motion is governed by a *singular* equation involving the derivatives of the solution:

$$\dot{\chi}(t) = \Xi(\partial_t \mathbf{v}_{|\chi}(t), \partial_x \mathbf{v}_{|\chi}(t)).$$

This case is illustrated by the study of wave interaction with a partly immersed obstacle locally placed over the free-surface, constraining the flow from above in some given area. The position of the obstacle does not vary over time, but the location of the air-water-object contact points does, due to changes in the flow configuration. This study also paves the way towards a more elaborated model embedding some floating objects that may also move over time.

To achieve this, a suitable mapping between the initial (reference) configuration and the current (time-varying) one is introduced and the NSW equations are recast into the reference domain, with the introduction of additional geometric terms related to the grid's motion, before being approximated by our DG method. As it is well-known that the solution of nonlinear hyperbolic equations encounters some loss of regularity in finite time and high-order DG methods may produce spurious oscillations in the vicinity of the solution's singularities (discontinuities, steeply varying gradients or dry areas for fee-surface flows), stabilization strategies have to be considered to enforce the required nonlinear stability, let mention [8] for the description of a widely used slope-limiter. However, using limiters may prevent from converging towards steady-states and also negatively impact the overall accuracy. Recently in [17], we designed an arbitrary-order DG approximation for the NSW equations with *a posteriori* Local Sub-cell Correction (LSC), which relies on lowest-order corrected fluxes, operating on a dedicated sub-partition. This particular sub-cell correction has been initially designed in [32] for systems of conservation laws on 1D and 2D Cartesian geometries, and extended to 2D unstructured meshes in [33]. This method has proved to be extremely robust, while retaining the accuracy of the high-order polynomial description and coming with appealing sub-mesh resolution capabilities. Hence, another objective of this paper is to extend the stabilization operator of [17] to the proposed DG-ALE framework. This stabilization procedure also comes with suitable local conservative variables reconstructions borrowed from [24], ensuring that robustness and well-balancing (for motionless steady-states) are embedded properties of the limit lowest-order scheme.

It worth mentioning [20, 15] where DG schemes, solving different NSW system of equations, have been developed and combined, similarly to [17], with an *a posteriori* sub-cell correction based a robust lower order scheme. Let us emphasize that, while these stabilization procedures are indeed close related, the one presented in this article is local to the subcell, and thus enables a better preservation of the very precise subcell resolution of DG scheme, see [32] for a comparison between the two.

Within ALE simulations of flows with moving boundaries, it is also important to ensure that a numerical scheme exactly reproduces any constant solution. The Geometric Conservation Law (GCL) is a relation between the ALE mapping's jacobian and the mesh velocity, stating that a uniform flow should not be influenced by any arbitrary grid's motion. The notion of GCL was first introduced in [28] and is also discussed in [25, 26] and [16], where relations between GCL and stability are investigated. We prove that the stabilized DG-ALE formulation proposed in this paper ensures such a property, both at the semi-discrete level (GCL) and the fully discrete level (DGCL), hence successfully combining well-balancing

with geometric conservation.
The remainder of this work is structured as follows. In the next section, we introduce the governing models, based on the NSW equations for the fluid description. The discrete setting, as well as the numerical discretization in space and time, are described in §3. In particular, we discuss the ALE description and the corresponding mapping, the stabilization and robustness enforcement through the *a posteriori* LSC method and exploiting the fact that the proposed DG-ALE formulation can be regarded as a FV-like scheme on a sub-mesh with particular high-order interface fluxes, as done in [17]. The resulting ability of the stabilized DG-ALE setting to preserve the well-balancing property, as well as the DGCL, are also investigated. In §4, we show several numerical assessments of the global algorithms.

2 Free-surface shallow-water flow on a moving domain

In this section, we provide a general description of the two wave-structure interaction problems under study and recall the associated IBVPs introduced in [19], together with the corresponding well-posedness results, as a firm theoretical ground for the subsequent numerical investigations.

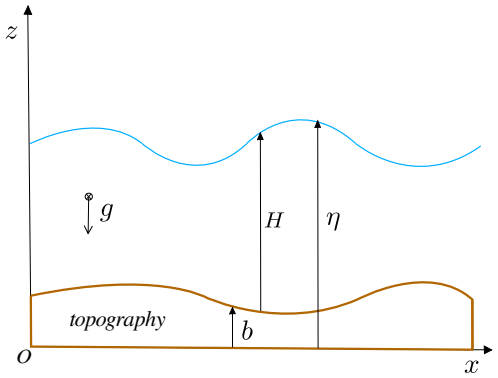

Fig. 1: Free-surface flows: main notations

In what follows, we consider an interval $\Omega_t \subset \mathbb{R}$, which is partitioned as $\Omega_t = \mathcal{E}(t) \cup \mathcal{I}(t)$, $\mathcal{E}(t)$ referring to the fluid domain and $\mathcal{I}(t)$ to the structure domain. We denote by $\partial\mathcal{E}(t)$ and $\partial\mathcal{I}(t)$ the respective boundaries of $\mathcal{E}(t)$ and $\mathcal{I}(t)$ and we note $\Gamma(t) = \partial\mathcal{E}(t) \cap \partial\mathcal{I}(t)$ the free-boundary. We consider the fluid evolution in $\mathcal{E}(t)$, described by the following free-boundary IBVP for the NSW equations defined on a moving domain:

$$\begin{cases} \partial_t \mathbf{v} + \partial_x \mathbf{F}(\mathbf{v}, b) = \mathbf{B}(\mathbf{v}, b'), & \text{in} \quad \mathcal{E}(t), & \text{(4a)} \\ \mathbf{v}_{|t=0} = \mathbf{v}^0, & \text{in} \quad \mathcal{E}(0) =: \mathcal{E}^0, & \text{(4b)} \\ \mathbf{v}_{|\Gamma(t)} = \mathbf{v}^{\mathrm{b}}, & \text{for} \quad t > 0, & \text{(4c)} \end{cases}$$

where: (i) the time-varying domain $\mathcal{E}(t)$ is specified below depending on the problem under study, (ii) the initial data $\mathbf{v}^0$ is assumed to belong to $H^s(\mathcal{E}^0)^2$, where $H^s(\mathcal{E})$ is the Sobolev space of functions $v \in L^2(\mathcal{E})$ such that their weak derivatives up to order s have a finite L^2-norm, (iii) the boundary condition $\mathbf{v}^{\mathrm{b}}$ and the corresponding boundary-evolution equation are also specified below. We emphasize that this is not a classical Dirichlet condition, as the boundary's definition depends on time. In what follows, the boundary data $\mathbf{v}^{\mathrm{b}}$ is provided as the result of the water interactions with a solid structure located in the neighboring domain $\mathcal{I}(t)$.
In the remainder of this section, we investigate two different situations, corresponding to the two types of free-boundary evolution equations mentioned in the introduction. In the first example, a horizontally moving piston is placed in $\mathcal{I}(t)$, the associated boundary-evolution is a kinematic-type relation and is computed as the solution of a second-order ordinary differential equation (ODE). In the second example, we investigate the occurence of a constraining surface-obstacle in $\mathcal{I}(t)$, the corresponding boundary-evolution is fully-nonlinear and the boundary data depends not only on the boundary's location, but also on an additional variable $\underline{q^{\mathrm{i}}}$ which is itself defined as the solution of a nonlinear first-order ODE.

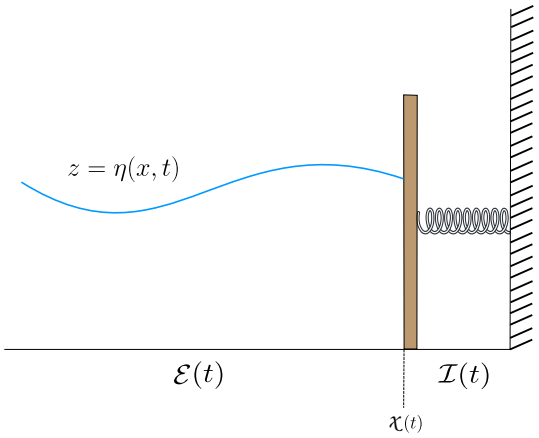

Fig. 2: Flow interacting with a lateral piston

2.1 Flow interacting with a lateral piston

In a first configuration, we consider the half-line $\mathcal{E}(t) := (-\infty, \chi(t))$, delimited from the right by a lateral piston placed in $\mathcal{I}(t)$, which can move in the horizontal direction, so that the free-boundary reduces to a single point $\Gamma(t) = \{\chi(t)\}$, see Fig. 2. When the motion is enforced, this models a piston-paddle device, used for instance in wave-tanks to generate incident waves and study coastal structures. When the wall is allowed to move according to the waves pressure, this displacement extends or compresses a spring which tends to bring the piston back to its equilibrium position, mimicking for instance a simplified mechanical response of a shore-mounted wave-energy absorber, see Fig. 2. This configuration is numerically studied for instance in [22,21] using potential flow models and a semi-analytical numerical methods. Within this configuration, a suitable definition of the boundary condition (4c) should enforce the following identity between the fluid velocity and the piston motion:

$$u_{|x=\chi} = \dot{\chi}, \tag{5}$$

which may also, reversely, be regarded as a kinematic-type boundary-evolution equation. To explicitly compute $\dot{\chi}$, the fluid evolution should be combined with the Newton's equation satisfied by the wall's position, which may be formulated as follows:

$$\begin{cases} m\ddot{\chi} &= -k(\chi - X^0) + \dfrac{1}{2}\rho g\left(\eta(\chi,\cdot)^2 - H_0^2\right), & \text{(6a)} \\ (\chi, \dot{\chi})_{|t=0} := (X^0, \dot{X}^0), & \text{(6b)} \end{cases}$$

where m is the mass of the moving piston, k the stiffness of the spring, $(X^0, \dot{X}^0)$ the initial location and velocity of the piston, ρ the water density and H_0 the mean water-depth. Denoting by $\mathcal{E}^0 := (-\infty, X^0)$ the initial domain, and given compatibility conditions (essentially assuming that the flow is initially subcritical and the system is initially in equilibrium), it is shown in [19] that there exists a maximal time $T_{\max}$ such that the coupled free-boundary problem (4)-(5)-(6) has a unique solution $\mathbf{v} \circ \chi \in \mathcal{C}^0\left([0, T_{\max}]; H^s(\mathcal{E}^0)\right) \cap \mathcal{C}^1\left([0, T_{\max}]; H^{s-1}(\mathcal{E}^0)\right)$, $\chi \in H^{s+2}(0, T_{\max})$, where χ, is a smooth mapping applying from the initial domain $\mathcal{E}^0$ to the current one $\mathcal{E}(t)$ and explicitly defined in [19].

2.2 Flow interacting with a surface-obstacle

In the second problem, we consider the NSW equations with a partly immersed obstacle placed locally over the surface, constraining the flow from above in some given area, under the assumptions that there are only two contact-points where the water, the air, and the obstacle meet, and that wave overtopping do not occur, see Fig. 3. For any given time value $t \geq 0$, the horizontal spatial coordinate of these contact-points are denoted by $\chi_-(t)$ and $\chi_+(t)$, with $\chi_-(t) < \chi_+(t)$, allowing to split the horizontal line into two time-dependent sub-domains, namely the *interior* sub-domain corresponding to $\mathcal{I}(t)$, and the *exterior*

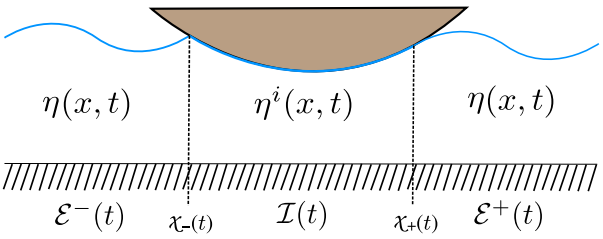

Fig. 3: Flow interacting with a surface-obstacle.

sub-domain $\mathcal{E}(t)$, $\mathcal{E}(t)$ and $\mathcal{I}(t)$ being the projections on the horizontal line of the areas where the water surface get in touch with the obstacle and the air:

$$\mathcal{E}(t) := \mathcal{E}^-(t) \cup \mathcal{E}^+(t), \quad \mathcal{E}^-(t) := (-\infty, \chi_-(t)), \quad \mathcal{E}^+(t) := (\chi_+(t), +\infty), \quad \mathcal{I}(t) := (\chi_-(t),\, \chi_+(t)), \tag{7}$$

and the corresponding free-boundary is defined as $\Gamma(t) = \{\chi_-,\, \chi_+\}$. The vector of flow variables in $\mathcal{I}(t)$ is denoted by $\mathbf{v}^{\mathrm{i}} := \big(\eta^i,\, q^i\big)$, and the corresponding water-height H^i is defined accordingly. In what follows, for any regular enough function $v(\cdot,t)$ defined on $\mathcal{I}(t)$, we introduce the following jump operator over the interior sub-domain:

$$[\![v]\!]_{\mathcal{I}(t)} := v(\chi_+(t),t) - v(\chi_-(t),t).$$

To determine the time-evolution of $\mathbf{v}^{\mathrm{i}}$, one may realize that: (i) η^i locally coincides with the parameterization of the obstacle's underside and does not explicitly depend on time (though it implicitly depends on time as $\mathcal{I}(t)$ does):

$$\eta^i(x,t) = \eta_{\mathrm{lid}}(x) \quad \text{on} \quad \mathcal{I}(t) \subset \mathcal{I}_{\mathrm{lid}}, \tag{8}$$

where $\eta_{\mathrm{lid}} \in \mathcal{C}^1(\mathcal{I}_{\mathrm{lid}})$ and $\mathcal{I}_{\mathrm{lid}}$ is the open interval where the parameterization of the obstacle's underside is defined, with $\mathcal{I}(0) \subset \mathcal{I}_{\mathrm{lid}}$, see Fig. 4, (ii) the discharge only depends on time and is ruled by a nonlinear ODE, as follows:

$$\forall x \in \mathcal{I}(t), \quad q^i(x,t) = \underline{q}^{\mathrm{i}}(t) \quad \text{with} \quad \dot{\underline{q}}^{\mathrm{i}} = -\Big(\int_{\mathcal{I}(t)} \frac{1}{H^i}\,\mathrm{d}x\Big)^{-1} \Big[\!\Big[\frac{1}{2}\Big(\frac{q^{\mathrm{i}}}{H^i}\Big)^2 + \mathrm{g}\eta^i\Big]\!\Big]_{\mathcal{I}(t)}. \tag{9}$$

The derivation of this ODE can be found in [19] and is also recalled in A for the sake of completeness. Assuming that $\mathbf{v}^{\mathrm{i}}(\cdot,t) = (\eta_{\mathrm{lid}|\mathcal{I}(t)},\, \underline{q}^{\mathrm{i}}(t))$ is known, the boundary condition (4c) is defined as follows:

$$\mathbf{v}^{\mathrm{b}} \;=\; \mathbf{v}^{\mathrm{i}}_{|\chi_\pm(t)}, \tag{10}$$

and the corresponding boundary-evolution equation is obtained by time-differentiating the first equation of (10) and using the fact that $\partial_t\eta = -\partial_x q$ and $\partial_t\eta^i = 0$:

$$\dot{\chi}_\pm = \left(\frac{\partial_x q}{\partial_x\eta - \partial_x\eta^i}\right)_{\big|\chi_\pm}. \tag{11}$$

Considering the initial partition $\mathcal{E}^0 \cup \mathcal{I}^0$ with

$$\mathcal{E}^0 := \mathcal{E}_0^- \cup \mathcal{E}_0^+, \quad \text{with} \quad \mathcal{E}_0^- := (-\infty, X_-^0), \quad \mathcal{E}_0^+ := (X_+^0, +\infty), \quad \mathcal{I}^0 := (X_-^0\ ,\ X_+^0), \tag{12}$$

where $X_\pm^0$ are the initial locations of the contact-points, see Fig. 4, and considering the initial data $\underline{q}^{\mathrm{i}}_{|t=0} := \underline{q}^{\mathrm{i},0} \in \mathbb{R}$, a local well-posedness result is also stated in [19], with additional assumptions ensuring that: (i) no dry-state occurs in the vicinity of the obstacle, (ii) the flow is initially sub-critical at the boundaries, (iii) the first-order spatial derivative of the free-surface is singular at the contact-points:

$$(\eta^0 - \eta_{\mathrm{lid}})' \neq 0 \qquad \text{at} \quad X_\pm^0, \tag{13}$$

and (iv) η_{lid} and its weak derivatives up to order s are uniformly bounded, then there exists a maximum time $T_{\max}$ and a unique solution of the coupled problem (4)-(9)-(10) such that $\mathbf{v}\circ\chi \in \mathcal{C}^0\left([0,T_{\max}]; H^s(\mathcal{E}^0)\right) \cap \mathcal{C}^1\left([0,T_{\max}]; H^{s-1}(\mathcal{E}^0)\right)$, $\underline{q}^{\mathrm{i}} \in H^{s+1}(0,T_{\max})$, $(\chi_-,\chi_+) \in (H^s(0,T_{\max}))^2$, where χ is a diffeomorphism, applying from the initial domain $\mathcal{E}^0$ to the current one $\mathcal{E}(t)$, defined in [19] and recalled in (47).

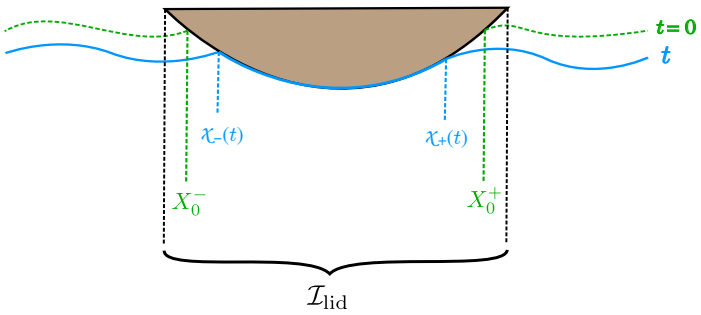

Fig. 4: Water interacting with a surface obstacle.

Remark 1 In the remainder of this work, we consider such IBVPs located on bounded computational domains of the form $\Omega_t := \mathcal{E}(t) \cup \mathcal{I}(t)$, with

$$\mathcal{E}(t) := \big(x_{\text{left}}, \chi(t)\big),$$

for the first problem (4)-(5)-(6), and

$$\mathcal{E}(t) := \big(x_{\text{left}},\, \chi_-(t)\big) \cup \big(\chi_+(t),\, x_{\text{right}}\big),$$

for the second problem (4)-(9)-(10), so that additional boundary conditions on $\mathbf{v}_{|x_{\text{left}}}$ and/or $\mathbf{v}_{|x_{\text{right}}}$ may be needed depending on the flow regime, and we conveniently denote by

$$\partial\Omega_t := \partial\mathcal{E}(t) \backslash \Gamma(t) \tag{14}$$

the boundary of the flow domain $\mathcal{E}(t)$ which is not connected to $\mathcal{I}(t)$, so that $\partial\Omega_t = \{x_{\text{left}}\}$ for the wave-piston problem and $\partial\Omega_t = \{x_{\text{left}}, x_{\text{right}}\}$ for the wave-obstacle problem. In the test-cases of §4, homogeneous Neumann and/or Dirichlet boundary conditions are weakly enforced on $\partial\Omega_t$, see also Remark 10.

3 Discrete formulations

In this section, we introduce numerical methods that approximate the solutions of the free-boundary problems (4)-(5)-(6) and (4)-(9)-(10).

3.1 Discrete setting for DG-ALE on cells and FV-ALE on sub-cells

Computational domain, sub-domains and mesh

We consider an open bounded domain $\Omega_t := \left]x_{\text{left}},\, x_{\text{right}}\right[$ and, for any time value $t \in [0, T_{\max}]$, we introduce a partition $\mathcal{P}_\Omega(t) := \{\mathcal{E}(t), \mathcal{I}(t)\}$ of Ω_t into disjoint sub-domains, $\mathcal{E}(t)$ being the domain on which the NSW equations are defined. The definition of $\mathcal{P}_\Omega(t)$ is related to the knowledge of the boundary $\Gamma(t) := \partial\mathcal{E}(t) \cap \partial\mathcal{I}(t)$ and with the notations of the previous section, we have $\Gamma(t) = \{\chi(t)\}$ for the wave-piston problem of §2.1, and $\Gamma(t) = \{\chi_-(t), \chi_+(t)\}$ for the wave-obstacle problem of §2.2.

We introduce a conforming mesh $\mathscr{T}_h^e(t) := \big\{c_i(t)\big\}_{1 \le i \le n_{\text{el}}}$ of $\mathcal{E}(t)$ into $|\mathscr{T}_h^e(t)|$ disjoint segments, such that we have $\overline{\mathcal{E}(t)} = \bigcup_{c(t) \in \mathscr{T}_h^e(t)} \overline{c(t)}$.
For any specified mesh element $c_i(t) \in \mathscr{T}_h^e(t)$, we note $c_i(t) = \left]x_{i-\frac{1}{2}}(t),\, x_{i+\frac{1}{2}}(t)\right[$ (with the suitable adaptation at the boundary), $x_i(t)$ refers to its barycenter, and for any regular enough function $v(\cdot, t)$ defined on $c_i(t)$, we define the following cell-jump operator:

$$\big[\!\big[v(\cdot,t)\big]\!\big]_{\partial c_i(t)} := v(\cdot,t)_{|x_{i+\frac{1}{2}}(t)} - v(\cdot,t)_{|x_{i-\frac{1}{2}}(t)}.$$

DG: approximation spaces, basis functions and projectors

For any integer $k \geq 0$, we consider the broken-polynomials space defined on $\mathcal{E}(t)$:

$$\mathbb{P}^k(\mathscr{T}_h^e(t)) := \left\{ v(\cdot,t) \in L^2(\mathcal{E}(t)),\ \ v_{|c(t)} \in \mathbb{P}^k(c(t)),\ \ \forall\, c(t) \in \mathscr{T}_h^e(t) \right\},$$

where $\mathbb{P}^k(c(t))$ denotes the space of polynomials of total degree at most k defined onto $c(t)$, with $\dim\left(\mathbb{P}^k(c(t))\right) = k+1$. Piecewise polynomial functions belonging to $\mathbb{P}^k(\mathscr{T}_h^e(t))$ are denoted with a subscript h in the following, and for any $c(t) \in \mathscr{T}_h^e(t)$ and $v_h(\cdot,t) \in \mathbb{P}^k(\mathscr{T}_h^e(t))$, we may use the convenient shorthand: $v_c := v_{h|c}$ when no confusion is possible.

For any cell $c(t) \in \mathscr{T}_h^e(t)$ and any integer $k \geq 0$, we consider a basis for $\mathbb{P}^k(c(t))$ denoted by

$$\Psi_c(t) := \left\{ \psi_m^c(\cdot,t) \right\}_{m \in [\![1,\, k+1]\!]},$$

such that we have:

$$\forall t \in [0, T_{\max}], \quad \forall c(t) \in \mathscr{T}_h^e(t), \quad \forall m \in [\![1, k+1]\!], \quad \operatorname{supp}(\psi_m^c(\cdot,t)) \subset \overline{c(t)}.$$

Gathering the local basis functions gives a basis for $\mathbb{P}^k(\mathscr{T}_h^e(t))$:

$$\Psi_h(t) := \bigtimes_{c(t) \in \mathscr{T}_h^e(t)} \Psi_c(t) = \left\{ \left\{ \psi_m^c(\cdot,t) \right\}_{m \in [\![1,\, k+1]\!]} \right\}_{c(t) \in \mathscr{T}_h^e(t)}.$$

Remark 2 In what follows, we set

$$\forall c_i(t) \in \mathscr{T}_h^e(t),\ \forall m \in [\![1, \ldots, k+1]\!],\ \forall x \in c_i(t), \quad \psi_m^{c_i}(x,t) := \left(\frac{x - x_i(t)}{|c_i(t)|} \right)^m. \tag{15}$$

For any given time value, the degrees of freedom are chosen to be the functionals that map a given discrete unknown belonging to $\mathbb{P}^k(\mathscr{T}_h^e(t))$ to the coefficients of its expansion on the chosen basis functions. Specifically, the degrees of freedom applied to a given function $v_h \in \mathbb{P}^k(\mathscr{T}_h^e(t))$ return the real numbers

$$\left\{ \underline{v}_m^c \right\}_{\substack{m \in [\![1,\, k+1]\!] \\ c \in \mathscr{T}_h^e(t)}}, \quad \text{such that} \quad v_c := \sum_{m=1}^{k+1} \underline{v}_m^c \psi_m^c, \quad \forall c \in \mathscr{T}_h^e(t). \tag{16}$$

With a little abuse, we refer hereafter to the real numbers (16) as the *degrees of freedom* associated with v_h and we note $\underline{v}_c \in \mathbb{R}^{k+1}$ the vector gathering the degrees of freedom associated with v_c.

For $c(t) \in \mathscr{T}_h^e(t)$, we denote by p_c^k the L^2-orthogonal projector onto $\mathbb{P}^k(c(t))$ and $\mathrm{p}_{\mathscr{T}_h^e}^k$ the L^2-orthogonal projector onto $\mathbb{P}^k(\mathscr{T}_h^e(t))$. Similarly, we denote I_c^k the element nodal interpolator into $\mathbb{P}^k(c(t))$, where the nodal distributions in mesh elements are chosen to be the approximate optimal nodes of [7]. The global $\mathrm{I}_{\mathscr{T}_h^e}^k$ interpolator into $\mathbb{P}^k(\mathscr{T}_h^e(t))$ is obtained by gathering the local interpolating polynomials defined on each elements. We also introduce the following shorthand notations for smooth scalar-valued functions:

$$\left(v, w\right)_{\mathscr{T}_h^e(t)} := \sum_{c(t) \in \mathscr{T}_h^e(t)} \int_{c(t)} v(x,t) w(x,t) \mathrm{d}x, \quad \left\langle \mu, \nu \right\rangle_{\partial \mathscr{T}_h^e(t)} := \sum_{c(t) \in \mathscr{T}_h^e(t)} [\![\mu \nu]\!]_{\partial c(t)},$$

for $v, w \in L^2(\mathscr{T}_h^e)$ and $\mu, \nu \in L^2(\partial \mathscr{T}_h^e)$. Extensions to vector-valued functions are straightforward.

Remark 3 Strictly speaking, the definition of a discrete setting onto $\mathcal{I}(t)$ is not mandatory. However, for the wave-obstacle problem (4)-(9)-(10), integrals over $\mathcal{I}(t)$ should be computed to solve (9): quadrature rules are needed, and as $\mathcal{I}(t)$ is a moving domain, such rules should move accordingly. A convenient implementation strategy is to introduce: (i) a partition $\mathscr{T}_h^i(t)$ of $\mathcal{I}(t)$ such that $\overline{\mathcal{I}(t)} = \bigcup_{c(t) \in \mathscr{T}_h^i(t)} \overline{c(t)}$, (ii) piecewise-polynomial interpolation onto $\mathbb{P}^k(\mathscr{T}_h^i(t))$ together with the corresponding projectors $\mathrm{p}_{\mathscr{T}_h^i(t)}^k$ and interpolators $\mathrm{I}_{\mathscr{T}_h^i}^k$. Then, global partitions of the whole computational domain Ω_t are obtained as the disjoint union $\mathscr{T}_h(t) := \mathscr{T}_h^e(t) \cup \mathscr{T}_h^i(t)$ and the global polynomial spaces $\mathbb{P}^k(\mathscr{T}_h(t))$, projectors $\mathrm{p}_{\mathscr{T}_h}^k$ and interpolators $\mathrm{I}_{\mathscr{T}_h}^k$ are defined accordingly.

FV on sub-cells: sub-partitions, sub-resolution basis and sub-mean values

For any mesh element $c_i(t) \in \mathscr{T}_h^e(t)$, we introduce a sub-partition $\mathscr{T}_{c_i(t)}$ into $k+1$ open disjoint sub-cells:

$$\overline{c_i(t)} = \bigcup_{m=1}^{k+1} \overline{s}_m^{c_i}(t), \tag{17}$$

where the sub-cell $s_m^{c_i}(t) := \left[\widetilde{x}_{m-\frac{1}{2}}^{c_i}(t), \widetilde{x}_{m+\frac{1}{2}}^{c_i}(t)\right]$ is of size $\left|s_m^{c_i}\right| = \left|\widetilde{x}_{m+\frac{1}{2}}^{c_i} - \widetilde{x}_{m-\frac{1}{2}}^{c_i}\right|$, with the convention $\widetilde{x}_{\frac{1}{2}}^{c_i} = x_{i-\frac{1}{2}}$ and $\widetilde{x}_{k+\frac{3}{2}}^{c_i} = x_{i+\frac{1}{2}}$, see Fig. 5. When considering a sequence of neighboring mesh elements c_{i-1}, c_i, c_{i+1}, the convenient conventions $s_0^{c_i} := s_{k+1}^{c_{i-1}}$ and $s_{k+2}^{c_i} := s_1^{c_{i+1}}$ may be used. For any regular enough function $v(\cdot,t)$ defined on $s_m^c(t)$, we use the following shorthand for the sub-cell jump:

$$\left[\!\left[v(\cdot,t)\right]\!\right]_{\partial s_m^c(t)} := v(\cdot,t)_{|\widetilde{x}_{m+\frac{1}{2}}^c(t)} - v(\cdot,t)_{|\widetilde{x}_{m-\frac{1}{2}}^c(t)}.$$

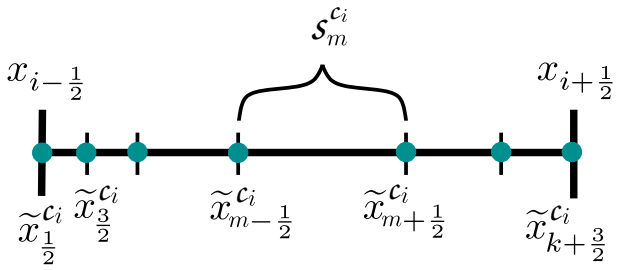

Fig. 5: Partition of a mesh element c_i in $k+1$ sub-cells

For $c(t) \in \mathscr{T}_h^e(t)$, we define the *sub-cell indicator* functions $\left\{\mathbb{1}_m^c(\cdot,t),\ m \in [\![1,\, k+1]\!]\right\}$ as follows:

$$\mathbb{1}_m^c(x,t) := \begin{cases} 1 & \text{if } x \in s_m^c(t) \\ 0 & \text{if } x \notin s_m^c(t) \end{cases}, \quad \forall m \in [\![1,\, k+1]\!],$$

and the *sub-resolution* basis functions $\left\{\phi_m^c(\cdot,t) \in \mathbb{P}^k(c(t)),\ m \in [\![1,\, k+1]\!]\right\}$ as follows:

$$\phi_m^c(\cdot,t) := p_c^k\left(\mathbb{1}_m^c(\cdot,t)\right), \quad \forall m \in [\![1,\, k+1]\!]. \tag{18}$$

One can check that this definition also entails that for any given value of t:

$$\int_{c(t)} \phi_m^c \psi \mathrm{d}x = \int_{s_m^c(t)} \psi \mathrm{d}x, \quad \forall \psi \in \mathbb{P}^k\left(c(t)\right). \tag{19}$$

For any $c(t) \in \mathscr{T}_h^e(t)$, we consider the set of piecewise-constant functions on the sub-grid:

$$\mathbb{P}^0(\mathscr{T}_c(t)) := \left\{v(\cdot,t) \in L^2(c(t)),\ \ v_{|s_m^c(t)} \in \mathbb{P}^0(s_m^c(t)),\ \ \forall\, s_m^c(t) \in \mathscr{T}_c(t)\right\},$$

and for $v_c \in \mathbb{P}^k(c(t))$, we consider the collection $\left\{\overline{v}_m^c\right\}_{m \in [\![1,\, k+1]\!]}$ of the lowest-order piecewise-constant components, defined as the mean-values of v_c on the sub-cells belonging to the subdivision $\mathscr{T}_c(t)$, and called *sub-mean values* in the following. Such sub-mean values are gathered in a vector $\overline{v}_c \in \mathbb{R}^{k+1}$. Whenever a sequence of neighboring mesh elements c_{i-1}, c_i, c_{i+1} and associated neighboring approximations is considered, the following convenient convention may be used: $\overline{v}_0^{c_i} := \overline{v}_{k+1}^{c_{i-1}}$ and $\overline{v}_{k+2}^{c_i} := \overline{v}_1^{c_{i+1}}$.

Remark 4 Any polynomial $v_c \in \mathbb{P}^k(c)$ may be equivalently written either as a collection of degrees of freedom $\underline{v}^c$, or as a collection of sub-means values $\overline{v}_c$. Considering the local transformation matrix

$$\Pi_c = \left(\pi_{m,p}^c\right)_{m,p} \quad \text{with} \quad \pi_{m,p}^c = \frac{1}{|s_m^c(t)|} \int_{s_m^c(t)} \psi_p^c \mathrm{d}x, \qquad \forall\, (m,p) \in [\![1,\, k+1]\!]^2, \tag{20}$$

the following identities hold:

$$\boldsymbol{\Pi}_c\, \underline{v}_c = \overline{v}_c \quad \text{and} \quad \boldsymbol{\Pi}_c^{-1}\, \overline{v}_c = \underline{v}_c.$$

For further use, let also define the (one-to-one) projector onto the piecewise constant sub-grid space:

$$\begin{aligned} \pi^k_{\mathscr{T}_c} \colon \mathbb{P}^k(c(t)) &\to \mathbb{P}^0(\mathscr{T}_c(t)) \\ v_h^c &\mapsto \pi^k_{\mathscr{T}_c}(v_h^c) := \overline{v}_c. \end{aligned} \tag{21}$$

Time discretization

Concerning time discretization, for a given final computational time $T_{\max} > 0$, we consider a partition $(t^n)_{0\le n\le N}$ of the time interval $[0, T_{\max}]$ with $t^0 := 0$, $t^N := T_{\max}$ and $t^{n+1} - t^n =: \Delta t^n$. Details on the computation of the time step Δt^n, related to the choice of the time marching algorithms and some stability requirements, are given in § 3.8. For any sufficiently regular function of time w, we set $w^n := w(t^n)$ and in what follows, such shorthands relying on a superscript n may be used with any time varying entity, which is evaluated at discrete time t^n. For instance, we set:

$$\mathcal{E}^n := \mathcal{E}(t^n),\ \mathcal{I}^n := \mathcal{I}(t^n),\ \mathscr{T}_h^n := \mathscr{T}_h(t^n).$$

3.2 ALE description

In this section, we introduce an ALE description of the free-boundary problems (4)-(5)-(6) (wave-piston interactions) and (4)-(9)-(10) (wave-obstacle interactions). A central aspect of any ALE description is the construction of a continuous and regular coordinate transformation, recasting the equations from the reference (initial) domain Ω_0 to the current one Ω_t:

$$\Omega_0 \times [0, T_{\max}] \ni (X, t) \mapsto x(X, t) \in \Omega_t, \tag{22}$$

where X refers to the *reference* coordinate and $x := x(X, t)$ the associated *physical* coordinate. Such mapping is specified in the next sub-section. Anticipating on its definition, and further assuming its continuous differentiability with respect to time, piecewise-continuous differentiability with respect to X, and denoting by $v_{\mathrm{g}}(x, t)$ the grid's velocity at the physical point $x := x(X, t)$, the following identity holds:

$$v_{\mathrm{g}}(x(X, t), t) = \partial_t x(X, t). \tag{23}$$

Then, for any regular enough function $v(x, t)$, denoting by $\widetilde{v}(X, t) := v\left(x(X, t), t\right)$ its counterpart defined on the reference frame, the fundamental ALE relation between the total time-derivative, the Eulerian time-derivative and the spatial-derivative reads as follows:

$$\frac{\mathrm{d}}{\mathrm{d}t} v\Big(x(X, t), t\Big) := \Big(\partial_t + v_{\mathrm{g}}\,\partial_x\Big) v(x(X, t), t) =: \partial_t \widetilde{v}(X, t). \tag{24}$$

Mapping and geometric parameters

For both problems, as a direct ALE formulation is adopted, the referential and grid velocity can be chosen totally arbitrarily. For instance, one can decide to use the fluid flow velocity to define the mesh displacement and deformation, and thus reaches a pseudo-Lagrangian regime, see §3.3. Another choice could be, starting from the velocity of the moving boundary $\Gamma(t)$, to define the mesh interfaces velocities to ensure a smooth grid deformation, hence avoiding any negative volume or crossing point, see §3.4. Now, temporarily assuming that the velocities $\left\{v_{\mathrm{g}_{|i+\frac{1}{2}}}(t)\right\}_{0\le i\le n_{\mathrm{el}}}$ of the mesh interfaces are available, their spatial locations $\left\{x_{i+\frac{1}{2}}(t)\right\}_{0\le i\le n_{\mathrm{el}}}$ can be updated by considering the following family of IVPs:

$$\begin{cases} \partial_t x(X_{i+\frac{1}{2}}, t) = v_{\mathrm{g}_{|i+\frac{1}{2}}}(t), \\ x(X_{i+\frac{1}{2}}, 0) \quad := X_{i+\frac{1}{2}}. \end{cases} \tag{25}$$

Then, a suitable definition for the mapping (22) is such that, for any $c_i(0) := \left]X_{i-\frac{1}{2}}, X_{i+\frac{1}{2}}\right[\in \mathscr{T}_h(0)$, $X \in c_i(0)$ and $t \in [0, T_{\max}]$:

$$x_{|c_i(0)}(X, t) := \frac{\left(X_{i+\frac{1}{2}} - X\right)}{|c_i(0)|} x_{i-\frac{1}{2}}(t) + \frac{\left(X - X_{i-\frac{1}{2}}\right)}{|c_i(0)|} x_{i+\frac{1}{2}}(t), \tag{26}$$

With this mapping at hand, the velocity of any physical points belonging to the moving frame can be deduced as follows:

Proposition 1 *The frame's velocity is such that, for all* $t \in [0, T_{\max}]$ *and all mesh element* $\mathfrak{c}_i(t) =]x_{i-\frac{1}{2}}(t), x_{i+\frac{1}{2}}(t)[\in \mathscr{T}_h^e(t)$*, we have:*

$$\forall x \in \mathfrak{c}_i(t),\ v_{\mathrm{g}|\mathfrak{c}_i(t)}(x,t) = \frac{\left(x_{i+\frac{1}{2}}(t) - x\right)}{|\mathfrak{c}_i(t)|} v_{\mathrm{g}_{|i-\frac{1}{2}}}(t) + \frac{\left(x - x_{i-\frac{1}{2}}(t)\right)}{|\mathfrak{c}_i(t)|} v_{\mathrm{g}_{|i+\frac{1}{2}}}(t). \tag{27}$$

Proof Deriving (26) with respect to time gives:

$$\widetilde{v}_{\mathrm{g}|\mathfrak{c}_i(0)}(X,t) = \frac{(X_{i+\frac{1}{2}} - X)}{|\mathfrak{c}_i(0)|} v_{\mathrm{g}_{|i-\frac{1}{2}}}(t) + \frac{(X - X_{i-\frac{1}{2}})}{|\mathfrak{c}_i(0)|} v_{\mathrm{g}_{|i+\frac{1}{2}}}(t). \tag{28}$$

The deformation gradient associated with the grid's motion is obtained as the Jacobian of this mapping. In particular, the following identities are satisfied:

$$\begin{aligned} \partial_X x(X,t)_{|\mathfrak{c}_i(t)} =: \mathcal{J}_{\mathfrak{c}_i(t)} &= \frac{|\mathfrak{c}_i(t)|}{|\mathfrak{c}_i(0)|}, \\ \partial_X^k x(X,t)_{|\mathfrak{c}_i(t)} &= 0,\ \forall k \geq 2, \end{aligned}$$

so that the mapping is invertible and orientation-preserving. Also, for any $(X_a, X_b) \in (\mathfrak{c}_i(0))^2$, we have:

$$x(X_b,t) = x(X_a,t) + (X_b - X_a)\mathcal{J}_{\mathfrak{c}_i(t)},$$

and in particular, we deduce (27).

Remark 5 From (23), we observe that $\mathcal{J}$ satisfies the following fundamental relation, generally referred to as Geometric Conservation Law (GCL):

$$\partial_t\, \mathcal{J}(X,t) = \mathcal{J}\, \partial_x v_{\mathrm{g}}(x(X,t),t). \tag{30}$$

Now, we state an important property satisfied by the basis and sub-resolution basis functions:

Proposition 2 *The basis functions, as well as the sub-resolution basis functions, follow the trajectories:*

$$\forall \mathfrak{c}_i(t) \in \mathscr{T}_h^e(t),\ \forall p \in [\![1, \ldots, k+1]\!], \qquad \frac{\mathrm{d}}{\mathrm{dt}}\, \psi_p^{\mathfrak{c}_i}(x(X,t),t) = 0. \tag{31}$$

$$\forall \mathfrak{c}_i(t) \in \mathscr{T}_h^e(t),\ \forall m \in [\![1, \ldots, k+1]\!], \qquad \frac{\mathrm{d}}{\mathrm{dt}}\, \phi_m^{\mathfrak{c}_i}(x(X,t),t) = 0. \tag{32}$$

Proof We have:

$$\psi_p^{\mathfrak{c}_i}(x,t) = \psi_p^{\mathfrak{c}_i}(x(X,t),t) = \left(\frac{\mathcal{J}(X - X_i)}{\mathcal{J}|\mathfrak{c}_i(0)|}\right)^p = \left(\frac{X - X_i}{|\mathfrak{c}_i(0)|}\right)^p = \widetilde{\psi}_p^{\mathfrak{c}_i}(X),$$

and thus (31) is ensured. In a similar way, the property for the sub-resolution basis derives from the piecewise linearity of the mapping. Indeed, we have $\phi_m^{\mathfrak{c}}(x(X,t),t) = \widetilde{\phi}_m^{\mathfrak{c}(0)}(X)$, where

$$\widetilde{\phi}_m^{\mathfrak{c}(0)} := \mathrm{p}_{\mathfrak{c}(0)}^k(\mathbb{1}_m^{\mathfrak{c}(0)}), \quad \forall m \in [\![1,\, k+1]\!], \tag{33}$$

which directly implies (32).

Remark 6 Multiplying (4) by any $\psi(.,t) \in \mathbb{P}^k(\mathscr{T}_h^e(t))$ satisfying $\dfrac{\mathrm{d}}{\mathrm{dt}}\psi(x(X,t),t) = 0$, and integrating over $c_i(t)$ gives:

$$\int_{c_i(t)} \psi\, \partial_t \mathbf{v}\, \mathrm{d}x + \int_{c_i(t)} \psi\, \partial_x \mathbf{F}(\mathbf{v}, b)\, \mathrm{d}x = \int_{c_i(t)} \psi\, \mathbf{B}(\mathbf{v}, b')\, \mathrm{d}x. \tag{34}$$

We observe that (30) and (31) lead to the following identity:

$$\frac{\mathrm{d}}{\mathrm{dt}} \int_{c_i(t)} \mathbf{v}\, \psi\, \mathrm{d}x = \int_{c_i(t)} \psi\, \partial_t \mathbf{v}\, \mathrm{d}x + \int_{c_i(t)} \psi\, \partial_x (\mathbf{v} v_{\mathrm{g}})\, \mathrm{d}x,$$

and (34) becomes:

$$\frac{\mathrm{d}}{\mathrm{dt}} \int_{c_i(t)} \mathbf{v}\, \psi\, \mathrm{d}x + \int_{c_i(t)} \psi\, \partial_x \mathbf{G}(\mathbf{v}, b, v_{\mathrm{g}})\, \mathrm{d}x = \int_{c_i(t)} \psi\, \mathbf{B}(\mathbf{v}, b')\, \mathrm{d}x, \tag{35}$$

where we have set $\mathbf{G}(\mathbf{v}, b, v_{\mathrm{g}}) := \mathbf{F}(\mathbf{v}, b) - \mathbf{v} v_{\mathrm{g}}$. Another integration by parts gives:

$$\frac{\mathrm{d}}{\mathrm{dt}} \int_{c_i} \mathbf{v}\, \psi\, \mathrm{d}x - \int_{c_i} \mathbf{G}(\mathbf{v}, b, v_{\mathrm{g}})\, \partial_x \psi\ \mathrm{d}x + \left[\!\left[\psi\, \mathbf{G}(\mathbf{v}, b, v_{\mathrm{g}})\right]\!\right]_{\partial c_i(t)} = \int_{c_i} \psi\, \mathbf{B}(\mathbf{v}, b')\, \mathrm{d}x, \tag{36}$$

which is the strong form of the variational formulation retained in the next sub-sections.

3.3 DG-ALE formulation for the wave-piston model

In this sub-section, we introduce a semi-discrete formulation for the problem (4)-(5)-(6), under the assumptions of §2.1. This formulation reads: $\forall t \in]0, T_{\max}]$, find $\mathbf{v}_h(\cdot,t) \in \left(\mathbb{P}^k(\mathscr{T}_h^e(t))\right)^2$ and $\varkappa(t) \in \left]x_{\mathrm{left}}(t),\, x_{\mathrm{right}}(t)\right[$ such that, $\forall \varphi_h(\cdot,t) \in \mathbb{P}^k(\mathscr{T}_h^e(t))$ satisfying $\dfrac{\mathrm{d}}{\mathrm{dt}}\varphi_h(x(X,t),t) = 0$, the following system is satisfied:

$$\begin{cases} \dfrac{\mathrm{d}}{\mathrm{dt}}\left(\mathbf{v}_h, \varphi_h\right)_{\mathscr{T}_h^e(t)} + \left(\mathcal{A}_h(\mathbf{v}_h), \varphi_h\right)_{\mathscr{T}_h^e(t)} = 0, & \\ \mathbf{v}_h(\cdot,0) = \mathrm{p}^k_{\mathscr{T}_h^{e,0}}(\mathbf{v}^0), & \text{(37a)} \\ \mathbf{v}_{h|\varkappa} = \mathbf{v}^{\mathrm{b}}, & \\ m\ddot{\varkappa} = -\mathcal{k}(\varkappa - X^0) + \dfrac{1}{2}\rho g\left(\eta_{h|\varkappa}^2 - H_0^2\right), & \\ (\varkappa, \dot{\varkappa})_{|t=0} = (X^0, \dot{X}^0), & \text{(37b)} \\ b_h(\cdot,t) = \mathrm{I}^k_{\mathscr{T}_h(t)}(b), & \text{(37c)} \end{cases}$$

where:

(i) the discrete nonlinear operator $\mathcal{A}_h$ in (37a) is defined by

$$\left(\mathcal{A}_h(\mathbf{v}_h), \varphi_h\right)_{\mathscr{T}_h^e(t)} := -\left(\mathbf{G}(\mathbf{v}_h, b_h, v_{\mathrm{g}}), \partial_x^h \varphi_h\right)_{\mathscr{T}_h^e(t)} + \left\langle \mathbf{G}^\star, \varphi_h \right\rangle_{\partial \mathscr{T}_h^e(t)} - \left(\mathbf{B}(\mathbf{v}_h, b_h'), \varphi_h\right)_{\mathscr{T}_h^e(t)}, \tag{38}$$

$\mathbf{G}^\star$ being an interface numerical flux that approximates $\mathbf{F}(\mathbf{v}, b) - v_{\mathrm{g}}\mathbf{v}$ at an interior element boundary moving with the velocity v_{g}, and defined as

$$\mathbf{G}^\star := \mathbf{F}^\star - v_{\mathrm{g}} \mathbf{v}^\star,$$

where $\mathbf{F}^\star$ and $\mathbf{v}^\star$ are respectively consistent with $\mathbf{F}$ and $\mathbf{v}$, and computed with the global Lax-Friedrichs formula:

$$\mathbf{F}^\star(\mathbf{v}_R, \mathbf{v}_L, b_R, b_L) := \frac{1}{2}\left(\mathbf{F}(\mathbf{v}_R, b_R) + \mathbf{F}(\mathbf{v}_L, b_L) - \sigma(\mathbf{v}_R - \mathbf{v}_L)\right), \tag{39}$$

$$\mathbf{v}^\star(\mathbf{v}_R, \mathbf{v}_L, b_R, b_L) := \frac{1}{2}\Big(\mathbf{v}_R + \mathbf{v}_L - \frac{1}{\sigma}\left(\mathbf{F}(\mathbf{v}_R, b_R) - \mathbf{F}(\mathbf{v}_L, b_L)\right)\Big), \tag{40}$$

with $\sigma := \max_{c\in\mathscr{T}_h^e} \sigma_c$ and

$$\sigma_c := \max_{m\in[\![1,\,k+1]\!]} \left(\left| \overline{u}_m^c - \overline{v_{\mathrm{g}}}_m^c \right| + \sqrt{\mathrm{g}\overline{H}_m^c} \right), \tag{41}$$

(ii) the grid's velocity at the free-boundary is straightforwardly deduced from the kinematic-type boundary-evolution equation (5) and translates as follows:

$$v_{\mathrm{g}|\chi(t)} := \dot{\chi}. \tag{42}$$

Such a pseudo-Lagrangian description of the flow can also be used to define the velocity of any arbitrary grid interface, as follows:

$$v_{\mathrm{g}_{|i+\frac{1}{2}}}(t) := \frac{q^\star_{i+\frac{1}{2}}}{\eta^\star_{i+\frac{1}{2}} - b_{i+\frac{1}{2}}}, \quad \forall i = 1, ..., n_{\mathrm{el}}, \tag{43}$$

As seen in Proposition 5 and Section 4, this particular choice in the DG-ALE scheme will ensure that each cell has a constant mass through the fluid flow (Lagrangian behavior),

(iii) the boundary data $\mathbf{v}^{\mathrm{b}}$ is specified in order to simultaneously enforce a non-penetration condition at the free-boundary, mimicking the presence of a solid-wall corresponding to the piston, and ensure that the kinematic-type behavior of the boundary evolution is accurately translated at the discrete level. Recalling that the requested boundary condition is weakly enforced through the definition of the interface flux at the concerned boundary, this boils down to choose $\mathbf{v}^{\mathrm{b}}$ such that $\mathbf{G}^\star_{|\chi} = 0$. With the notations of (39)-(40), and assuming that $\mathbf{v}_L = \mathbf{v}_{h|\chi}$, we set

$$\mathbf{v}^{\mathrm{b}} = \left(\eta_L,\, q_L \left(\frac{v_{\mathrm{g}|\chi} - \sigma}{v_{\mathrm{g}|\chi} + \sigma} \right) + \left(\frac{2 v_{\mathrm{g}|\chi} \gamma}{v_{\mathrm{g}|\chi} + \gamma} \right) \eta_L \right), \tag{44}$$

and one may easily check that this formula reduces to the usual non-penetration condition at a stationary solid-wall when $v_{\mathrm{g}|\chi} = 0$, and that injecting $\mathbf{v}_L := \mathbf{v}_{h|\chi}$ and $\mathbf{v}_R := \mathbf{v}^{\mathrm{b}}$ into (39)-(40) leads to $(\mathbf{F}^\star - v_{\mathrm{g}}\mathbf{v}^\star)_{|\chi(t)} = 0$.

Remark 7 In (37c), the implicit time-dependency of b_h through its projection on the moving mesh is made explicit for the sake of clarity. Note that the interpolation of the smooth parameterization b into $\mathbb{P}^k(\mathscr{T}_h)$ is not mandatory, but it preserves the continuity of b at the mesh interfaces (provided that the elements boundary is included into the set of interpolation nodes) and allows to easily compute a polynomial approximation of its first-order derivative.

Remark 8 The eigenvalues and eigenvectors of the Jacobian matrix for $\mathbf{F}(\mathbf{v}, b) - \mathbf{v}v_{\mathrm{g}}$ are trivially obtained from the NSW system written in ALE description:

$$\frac{\partial \left(\mathbf{F}(\mathbf{v}, b) - \mathbf{v}v_{\mathrm{g}} \right)}{\partial \mathbf{v}}(\mathbf{v}, b) = \begin{pmatrix} v_{\mathrm{g}} & 1 \\ -u^2 + \mathrm{g}H & 2u - v_{\mathrm{g}} \end{pmatrix},$$

leading to eigenvalues that account for the frame velocity:

$$\lambda^\pm := u - v_{\mathrm{g}} \pm \sqrt{\mathrm{g}H}.$$

3.4 DG-ALE formulation for the wave / surface-obstacle model

Now, we consider the second problem (4)-(9)-(10) with the assumptions of §2.2. The associated DG-ALE semi-discrete formulation reads: $\forall t \in [0, T_{\max}]$, find $\mathbf{v}_h(\cdot, t) \in \left(\mathbb{P}^k(\mathscr{T}_h^e(t))\right)^2$, $\mathbf{v}_h^{\mathrm{i}}(\cdot, t) \in \mathbb{P}^k(\mathscr{T}_h^i(t)) \times \mathbb{P}^0(\mathscr{T}_h^i(t))$ and $(\chi_-(t), \chi_+(t)) \in \left]x_{\mathrm{left}}(t),\, x_{\mathrm{right}}(t)\right[^2$ such that, $\forall \varphi_h(\cdot, t) \in \mathbb{P}^k(\mathscr{T}_h^e(t))$ satisfying $\dfrac{\mathrm{d}}{\mathrm{d}t}\varphi_h(x(X,t),t) = 0$, the following system is satisfied:

$$
\begin{cases}
\dfrac{\mathrm{d}}{\mathrm{dt}}\big(\mathbf{v}_h,\varphi_h\big)_{\mathscr{T}_h^e(t)} + \big(\mathcal{A}_h(\mathbf{v}_h),\varphi_h\big)_{\mathscr{T}_h^e(t)} = 0, & \\
\mathbf{v}_{h|t=0} = \mathrm{p}^k_{\mathscr{T}_h^{e,0}}(\mathbf{v}^0), & \\
\mathbf{v}_{h|\mathcal{X}_\pm} = \mathbf{v}^{\mathrm{i}}_{h|\mathcal{X}_\pm}, &
\end{cases} \tag{45a}
$$

$$
\begin{cases}
\mathbf{v}^{\mathrm{i}}_h(\cdot,t) := \Big(\mathrm{p}^k_{\mathscr{T}^i_h(t)}(\eta_{\mathrm{lid}}), \underline{q}^{\mathrm{i}}(t)\Big), & \\
\dfrac{\mathrm{d}}{\mathrm{dt}}\underline{q}^{\mathrm{i}}(t) = -\Big(\displaystyle\int_{\mathcal{I}(t)} \frac{\mathrm{d}x}{H^i_h}\Big)^{-1} \Big[\!\Big[\frac{1}{2}\Big(\frac{\underline{q}^{\mathrm{i}}(t)}{H^i_h}\Big)^2 + \mathrm{g}\,\eta^i_h\Big]\!\Big]_{\mathcal{I}(t)}, & \\
\underline{q}^{\mathrm{i}}(0) = q^i_0, &
\end{cases} \tag{45b}
$$

$$
b_h(\cdot,t) = \mathrm{I}^k_{\mathscr{T}_h(t)}(b). \tag{45c}
$$

In order to specify the free-boundary velocity, we observe that the fully-nonlinear boundary-evolution equation (11) straightforwardly translates at the discrete level as:

$$
v_{\mathrm{g}|\mathcal{X}_\pm} = \frac{\partial_x q_{h|\mathcal{X}_\pm}}{\partial_x \eta_{h|\mathcal{X}_\pm} - \partial_x \eta^i_{h|\mathcal{X}_\pm}}, \tag{46}
$$

and, to additionally deduce the mesh interfaces velocity, we introduce the following smooth diffeomorphism from $\mathcal{E}^0$ to $\mathcal{E}(t)$:

$$
\chi(X,t) := \begin{cases}
X + \varphi\Big(\frac{X-X_0^-}{\varepsilon}\Big)\big(\mathcal{X}_-(t) - X_0^-\big) & \text{for} \quad X \in \mathcal{E}_0^-, \\
X + \varphi\Big(\frac{X-X_0^+}{\varepsilon}\Big)\big(\mathcal{X}_+(t) - X_0^+\big) & \text{for} \quad X \in \mathcal{E}_0^+,
\end{cases} \tag{47}
$$

where $\varphi \in \mathcal{C}^\infty_0(\mathbb{R})$ is a cut-off function satisfying $\varphi(x) = 1$ for $|x| \leq 1$ and $\varepsilon := \varepsilon_0 \ell$ (the reader is referred to B for the practical definition of φ, ε_0 and Remark 9 for additional considerations regarding the value of ℓ). Now, for any moving grid's interface $x_{i+\frac{1}{2}}(t) := x\big(X_{i+\frac{1}{2}}, t\big)$, we define the corresponding interface's velocity as follows:

$$
v_{\mathrm{g}_{|i+\frac{1}{2}}}(t) := \widetilde{v_{\mathrm{g}}}(X_{i+\frac{1}{2}}, t),
$$

with:

$$
\widetilde{v_{\mathrm{g}}}(X_{i+\frac{1}{2}}, t) := \begin{cases}
\partial_t \chi(\cdot,t)_{|X_{i+\frac{1}{2}}} \ \text{ if } \quad X_{i+\frac{1}{2}} \in \mathcal{E}^0, & \\
\dfrac{(X_0^+ - X_{i+\frac{1}{2}})}{|\mathcal{I}^0|} v_{\mathrm{g}|\mathcal{X}_-} + \dfrac{(X_{i+\frac{1}{2}} - X_0^-)}{|\mathcal{I}_0|} v_{\mathrm{g}|\mathcal{X}_+} \ \text{ if } \quad X_{i+\frac{1}{2}} \in \mathcal{I}^0. &
\end{cases} \tag{48}
$$

Remark 9 We emphasize that (47) offers a way to dispatch, at each time-step, the mesh elements into $\mathcal{E}(t)$, avoiding elements from collapsing, distorting and related stability issues. It is also worth highlighting that (47) allows to properly deal with the possible occurrence of dry-areas, provided that such areas are initially far enough from the surface-obstacle to prevent the water-height from vanishing at the free-boundary. Indeed, assuming that the distance between $\mathcal{X}_\pm(t)$ and the nearest mesh interface where the water height vanishes is greater than ℓ, then (47) ensures that this mesh interface location does not vary over time. This is numerically illustrated in §4.

Remark 10 The exterior boundary condition(s) on $\partial\Omega_t$ are not considered into the previous formulations, but are classically enforced weakly through the numerical fluxes $\mathbf{G}^\star$. On $\partial\Omega_t$, we may enforce any type of boundary conditions usually available for the NSW equations, including inflow and outflow conditions within subcritical or supercritical configurations relying on local Riemann invariants, periodic conditions or solid-wall conditions.

Remark 11 These two DG-ALE formulations still have to be supplemented with some stabilization, shock-capturing and reconstruction processes to ensure their robustness and handle the topography variations in a well-balanced way. These issues are addressed in the next sub-sections.

3.5 DG-ALE as a FV-ALE scheme on sub-cells

It is well-established that the DG formulations (37a) or (45a) need to be further stabilized in order to ensure the positivity of H_h at the discrete level, and to avoid Gibbs phenomenon in the vicinity of spatial singularities. In order to design some suitable correction mechanisms, we extend the *a posteriori* local sub-cell correction of DG schemes, developed for the NSW equations in [17], to the ALE framework. To do so, we adapt to the direct ALE frame the FV sub-cell reformulation of tDG method initially introduced in [32]. We follow the lines of [17] while highlighting the differences due to the frame's motion. Let introduce the following projections onto $\mathbb{P}^k\left(\mathscr{T}_h^e(t)\right)^2$:

$$\mathbf{F}_h^e := p^k_{\mathscr{T}_h^e(t)}\left(\mathbf{F}(\mathbf{v}_h, b_h)\right) \quad \text{and} \quad \mathbf{B}_h^e := p^k_{\mathscr{T}_h^e(t)}\left(\mathbf{B}(\mathbf{v}_h, b_h')\right), \tag{49}$$

together with the respective shorthands $\mathbf{F}_{c_i(t)} = \mathbf{F}^e_{h|c_i(t)}$, $\mathbf{B}_{c_i(t)} = \mathbf{B}^e_{h|c_i(t)}$, $\mathbf{G}_{c_i} = \mathbf{F}_{c_i} - v_{\mathrm{g}}\mathbf{v}_{c_i}$. We substitute these projections into (45a) and integrate by parts the second term to obtain, for all $\psi \in \mathbb{P}^k\left(\mathscr{T}_h^e(t)\right)$ satisfying $\dfrac{\mathrm{d}}{\mathrm{dt}}\psi\left(x(X,t),t\right) = 0$:

$$\frac{\mathrm{d}}{\mathrm{dt}}\int_{c_i(t)} \mathbf{v}_{c_i}\psi \,\mathrm{d}x = -\int_{c_i(t)} \partial_x \mathbf{G}_{c_i}\psi \,\mathrm{d}x + \left[\!\left[(\mathbf{G}_{c_i} - \mathbf{G}^\star)\psi\right]\!\right]_{\partial c_i(t)} + \int_{c_i(t)} \mathbf{B}_{c_i}\psi \,\mathrm{d}x. \tag{50}$$

For a given mesh element $c(t) \in \mathscr{T}_h^e(t)$, we consider a sub-partition $\mathscr{T}_c(t)$ defined in (17), together with the sub-resolution basis functions (18). Recalling that $\mathbf{v}_{c_i}$, $\partial_x(\mathbf{v}_{c_i} v_{\mathrm{g}})$, $\partial_x \mathbf{F}_{c_i}$ and $\mathbf{B}_{c_i}$ all belong to $\mathbb{P}^k\left(c_i(t)\right)^2$, the substitution of $\psi = \phi_m^{c_i}$ into (50) and the use of identity (19) enable us to derive the governing equations of the different sub-mean values $\overline{\mathbf{v}}_m^{c_i}$:

$$\frac{\mathrm{d}}{\mathrm{dt}}\left(|s_m^{c_i}(t)|\overline{\mathbf{v}}_m^{c_i}\right) = -\left[\!\left[\mathbf{G}_{c_i}\right]\!\right]_{\partial s_m^{c_i}(t)} + \left[\!\left[(\mathbf{G}_{c_i} - \mathbf{G}^\star)\phi_m^{c_i}\right]\!\right]_{\partial c_i(t)} + |s_m^{c_i}(t)|\,\overline{\mathbf{B}}_m^{c_i}. \tag{51}$$

We now introduce the $k+2$ sub-cell's *reconstructed fluxes*, denoted by $\left\{\widehat{\mathbf{G}}^{c_i}_{m+\frac{1}{2}}\right\}_{m\in[\![0,\,k+1]\!]}$, and defined as the solution of the following linear system:

$$\widehat{\mathbf{G}}^{c_i}_{m+\frac{1}{2}} - \widehat{\mathbf{G}}^{c_i}_{m-\frac{1}{2}} := \left[\!\left[\mathbf{G}_{c_i}\right]\!\right]_{\partial s_m^{c_i}(t)} - \left[\!\left[(\mathbf{G}_{c_i} - \mathbf{G}^\star)\phi_m^{c_i}\right]\!\right]_{\partial c_i(t)}, \quad \forall m \in [\![1,\,k+1]\!],$$

$$\widehat{\mathbf{G}}^{c_i}_{\frac{1}{2}} := \mathbf{G}^\star_{i-\frac{1}{2}} \qquad \text{and} \qquad \widehat{\mathbf{G}}^{c_i}_{k+3/2} := \mathbf{G}^\star_{i+\frac{1}{2}},$$

so that (45a) may be recast as a FV-ALE formulation on the sub-partition:

$$\frac{\mathrm{d}}{\mathrm{dt}}\left(|s_m^{c_i}(t)|\overline{\mathbf{v}}_m^{c_i}\right) = -\left(\widehat{\mathbf{G}}^{c_i}_{m+\frac{1}{2}} - \widehat{\mathbf{G}}^{c_i}_{m-\frac{1}{2}}\right) + |s_m^{c_i}(t)|\overline{\mathbf{B}}_m^{c_i}, \quad \forall m \in [\![1,\,k+1]\!]. \tag{52}$$

Remark 12 For practical purpose, an explicit formula for the computation of the interior reconstructed fluxes for $m \in [\![1,\ldots,k]\!]$ is:

$$\widehat{\mathbf{G}}^{c_i}_{m+\frac{1}{2}} = \mathbf{G}_{c_i}\left(\widetilde{x}_{m+\frac{1}{2}}\right) - c^{i-\frac{1}{2}}_{m+\frac{1}{2}}\left(\mathbf{G}_{c_i}\left(x_{i-\frac{1}{2}}\right) - \mathbf{G}^\star_{i-\frac{1}{2}}\right) - c^{i+\frac{1}{2}}_{m+\frac{1}{2}}\left(\mathbf{G}_{c_i}\left(x_{i+\frac{1}{2}}\right) - \mathbf{G}^\star_{i+\frac{1}{2}}\right), \tag{53}$$

with

$$c^{i-\frac{1}{2}}_{m+\frac{1}{2}} = \sum_{p=m+1}^{k+1} \phi_p^{c_i}\left(x_{i-\frac{1}{2}}\right) \qquad \text{and} \qquad c^{i+\frac{1}{2}}_{m+\frac{1}{2}} = \sum_{p=1}^{m} \phi_p^{c_i}\left(x_{i+\frac{1}{2}}\right). \tag{54}$$

Simple explicit expression of the correction coefficients can be found in [32].

Remark 13 We require that the integrals and source term in (45a) are exactly computed at motionless steady-states. This can be achieved, thanks to the pre-balanced formulation of the NSW equations, by using any quadrature rule that is exact for polynomials of degree up to $2\,k$. Let us recall that $2\,k$ is in any case the minimum requirement to reach the expected $k+1$ order of accuracy.

3.6 Sub-cell low-order corrected FV-ALE fluxes

In this section, we show that the reconstructed fluxes may be locally corrected to enforce some required properties. As investigated in [17] for the NSW equations, lowest-order FV fluxes may be introduced in order to: (i) prevent high-order approximations from spurious oscillations in the vicinity of discontinuities and sharp gradients, (ii) ensure the preservation of the water height's positivity. Additionally, one needs to introduce some states reconstructions, inspired from [24] in order to ensure a well-balancing property. In what follows, we recall the definition of such corrected fluxes, highlighting the new terms associated with the frame's motion.

For any time value $t \in [0, T_{\max}]$, $c_i(t) \in \mathscr{T}_h^e(t)$, and any marked sub-cell $s_m^{c_i}(t) \in \mathscr{T}_{c_i(t)}$, let define the sub-partition interface values for b, where the subscript c_i and the time dependency are forgotten for the sake of simplicity:

$$\overline{b}_{m+\frac{1}{2}} := \max(\overline{b}_m, \overline{b}_{m+1}), \quad \overline{b}_m^{\pm} := \overline{b}_{m\pm\frac{1}{2}} - \max\left(0, \overline{b}_{m\pm\frac{1}{2}} - \overline{\eta}_m\right).$$

sub-cell's interfaces reconstructions for the water height are defined as follows:

$$\overline{H}_m^{\pm} := \max\left(0, \overline{\eta}_m - \overline{b}_{m\pm\frac{1}{2}}\right),$$

and the corresponding free-surface elevation and discharge are deduced as follows:

$$\overline{\eta}_m^{\pm} := \overline{H}_m^{\pm} + \overline{b}_m^{\pm}, \qquad \overline{q}_m^{\pm} := \overline{H}_m^{\pm} \frac{\overline{q}_m}{\overline{H}_m}, \qquad \overline{\mathbf{v}}_m^{\pm} := (\overline{\eta}_m^{\pm}, \overline{q}_m^{\pm}), \tag{55}$$

where $\overline{b}_m^{\pm}$ refer to the trace of $\overline{b}_m$ at the sub-cell's interfaces. Related lowest-order numerical fluxes on sub-cell's $s_m(t)$ left and right interfaces are built accordingly:

$$\mathcal{F}_{m+\frac{1}{2}}^{l} := \mathbf{F}^{\star}\left(\overline{\mathbf{v}}_m^{+}, \overline{\mathbf{v}}_{m+1}^{-}, \overline{b}_m^{+}, \overline{b}_m^{+}\right) + \begin{pmatrix} 0 \\ \mathrm{g}\overline{\eta}_m^{+}\left(\overline{b}_m^{+} - b_{\widetilde{x}_{m+\frac{1}{2}}}\right) \end{pmatrix}, \tag{56}$$

$$\mathcal{F}_{m-\frac{1}{2}}^{r} := \mathbf{F}^{\star}\left(\overline{\mathbf{v}}_{m-1}^{+}, \overline{\mathbf{v}}_m^{-}, \overline{b}_m^{-}, \overline{b}_m^{-}\right) + \begin{pmatrix} 0 \\ \mathrm{g}\overline{\eta}_m^{-}\left(\overline{b}_m^{-} - b_{\widetilde{x}_{m-\frac{1}{2}}}\right) \end{pmatrix}, \tag{57}$$

where $b_{\widetilde{x}_{m\pm\frac{1}{2}}}$ are respectively the interpolated polynomial values of b_h at $\widetilde{x}_{m+\frac{1}{2}}$ and $\widetilde{x}_{m-\frac{1}{2}}$. The associated numerical flux, in the ALE description, are deduced as follows:

$$\mathcal{G}_{m+\frac{1}{2}}^{l} := \mathcal{F}_{m+\frac{1}{2}}^{l} - v_{\mathrm{g}_{|m+\frac{1}{2}}} \mathbf{v}_{m+\frac{1}{2}}^{\star,l}, \quad \text{and} \quad \mathcal{G}_{m-\frac{1}{2}}^{r} := \mathcal{F}_{m-\frac{1}{2}}^{r} - v_{\mathrm{g}_{|m-\frac{1}{2}}} \mathbf{v}_{m-\frac{1}{2}}^{\star,r}, \tag{58}$$

with

$$\mathbf{v}_{m+\frac{1}{2}}^{\star,l} := \mathbf{v}^{\star}\left(\overline{\mathbf{v}}_m^{+}, \overline{\mathbf{v}}_{m+1}^{-}, \overline{b}_m^{+}, \overline{b}_m^{+}\right), \quad \text{and} \quad \mathbf{v}_{m-\frac{1}{2}}^{\star,r} := \mathbf{v}^{\star}\left(\overline{\mathbf{v}}_{m-1}^{+}, \overline{\mathbf{v}}_m^{-}, \overline{b}_m^{-}, \overline{b}_m^{-}\right). \tag{59}$$

Using such corrected FV-ALE fluxes, it is possible to modify the reconstructed fluxes $\widehat{\mathbf{G}}_{m+\frac{1}{2}}$ in a robust way, in some particular sub-cells, where the *uncorrected* DG scheme (52) has failed to produce an admissible solution. We are thus left with the issues of identifying the local sub-cells that may need some corrections and defining a robust correction procedure, which are respectively addressed in §3.7 and §3.9.

3.7 Admissibility criteria

A large number of sensors or detectors have been introduced in the literature in order to identify the particular cells/sub-cells in which some additional stabilization mechanisms are required. We use two admissibility criteria: one for the *Physical Admissibility Detection* (PAD) and the other to address the occurrence of spurious oscillations, called *sub-cell Numerical Admissibility Detection* (SubNAD). This last criterion is supplemented with a relaxation procedure to exclude smooth extrema from the troubled cells. These criteria, which definitions are not recalled in the present work, are detailed in [17].

3.8 Time marching algorithm

So far, we only consider a semi-discrete spatial discretization. When fully-discrete formulations are considered, the time-stepping may be carried out using explicit Strong-Stability-Preserving Runge-Kutta (SSP-RK) schemes, [14,27], and following the notations introduced in §3.1, we denote the time-dependency on discrete time t^n with a superscript n:

$$\mathbf{v}_h^n := \mathbf{v}_h(\cdot, t^n), \quad \underline{q}^{\mathrm{i},n} := \underline{q}^{\mathrm{i}}(t^n), \quad \varkappa_{\pm}^n := \varkappa_{\pm}(t^n).$$

Writing the semi-discrete equation (45a) in the operator form

$$\partial_t \mathbf{v}_h + \mathcal{A}_h(\mathbf{v}_h) = 0,$$

we advance the discrete solution $\mathbf{v}_h^n \in \left(\mathbb{P}^k\left(\mathscr{T}_h^{e,n}\right)\right)^2$ from time level n to level $(n+1)$, with $\mathbf{v}_h^{n+1} \in \left(\mathbb{P}^k(\mathscr{T}_h^{e,n+1})\right)^2$, through the a SSP-RK scheme. Let us explicit the third-order RK case:

$$\begin{aligned}
\mathbf{v}_h^{n,(1)} &= \mathbf{v}_h^n - \Delta t^n \mathcal{A}_h(\mathbf{v}_h^n), \\
\mathbf{v}_h^{n,(2)} &= \frac{1}{4}(3\mathbf{v}_h^n + \mathbf{v}_h^{n,(1)}) - \frac{1}{4}\Delta t^n \mathcal{A}_h(\mathbf{v}_h^{n,(1)}), \\
\mathbf{v}_h^{n+1} &= \frac{1}{3}(\mathbf{v}_h^n + 2\mathbf{v}_h^{n,(2)}) - \frac{2}{3}\Delta t^n \mathcal{A}_h(\mathbf{v}_h^{n,(2)}),
\end{aligned}$$

where $\mathbf{v}_h^{n,(i)}$, $1 \leq i \leq 2$, are the solutions obtained at intermediate stages, Δt^n is obtained from the CFL condition (60). As the stability enforcement operator described in the previous sections relies on both DG approximations on mesh elements $c^n \in \mathscr{T}_h^{e,n}(t)$ and FV scheme on the sub-cells $s_m^{c,n} \in \mathscr{T}_c^n$, the time step Δt^n is computed adaptively using the following CFL condition:

$$\Delta t^n = \frac{\min\limits_{c^n \in \mathscr{T}_h^{e,n}} \left(\dfrac{h_c^n}{2k+1}, \min\limits_{s_m^{c,n} \in \mathscr{T}_c^n} |s_m^{c,n}| \right)}{\sigma}, \tag{60}$$

where σ is the constant previously introduced in (41). The same SSP-RK method for the discretization of equations of type (25) leads to the following discrete algorithm:

$$\begin{aligned}
x^{n,(1)} &= x^n + \Delta t^n v_{\mathrm{g}}^n, \\
x^{n,(2)} &= \frac{3x^n + x^{n,(1)}}{4} + \frac{\Delta t^n}{4} v_{\mathrm{g}}^{n,(1)}, \\
x^{n+1} &= \frac{x^n + 2x^{n,(2)}}{3} + \frac{2\Delta t^n}{3} v_{\mathrm{g}}^{n,(2)}.
\end{aligned} \tag{61}$$

3.9 *A posteriori* Local Sub-cell Correction (LSC) method

Gathering all the previous ingredients, we introduce a global algorithm that ensures the stability and robustness of the flow's computation in $\mathcal{E}(t)$. This algorithm is adapted from [17] and extended to the current DG-ALE framework. We only provide a qualitative description and focus on the steps that require further comments, due to the additional ALE description. Starting from an admissible piecewise polynomial approximate solution $\mathbf{v}_h^n \in \left(\mathbb{P}^k(\mathscr{T}_h^{\mathrm{e},n})\right)^2$ at discrete time t^n, we first compute a *predictor candidate solution* $\mathbf{v}_h^{n+1} \in \left(\mathbb{P}^k(\mathscr{T}_h^{\mathrm{e},n+1})\right)^2$ at time t^{n+1} using the uncorrected DG-ALE scheme (38), together with the corresponding SSP-RK time discretization of §3.8. Then, for any mesh element $c_i^{n+1} \in \mathscr{T}_h^{\mathrm{e},n+1}$, we compute the predictor candidate sub-mean values:

$$\mathbb{P}^0(\mathscr{T}_{c_i}^{\mathrm{e},n+1}) \ni \overline{\mathbf{v}}_{c_i}^{n+1} = \pi_{\mathscr{T}_{c_i}^{\mathrm{e},n+1}}(\mathbf{v}_{c_i}^{n+1}).$$

For any sub-cell $s_m^{c_i,n+1} \in \mathscr{T}_{c_i}^{n+1}$, we check admissibility of the associated sub-mean values $\overline{\mathbf{v}}_m^{c_i,n+1}$ using the criteria of §3.7. For a given sub-cell $s_m^{c_i,n+1}$ that needs additional stabilization, the corresponding DG *reconstructed interface fluxes* $\widehat{\mathbf{G}}_{m\pm\frac{1}{2}}$ defined in (53), which were initially used to compute the predictor candidate $\mathbf{v}_h^{n+1}$, will be replaced by the FV *corrected fluxes* $\mathcal{G}_{m\pm\frac{1}{2}}^{l/r}$ of (58) into the update process to

compute a new candidate sub-cell value through the local FV-ALE formulation (52). As we want the *a posteriori* LSC method to ensure conservation at the sub-cell level, the left and right sub-cells of a troubled one have to be also recomputed through a FV-like scheme but this time with possibly only one high-order reconstructed flux to be replaced by a first-order one. Let us emphasize that for the remaining sub-cells, nothing has to be done and their associated mean value will be the one obtained through the uncorrected DG scheme. For more details on the *a posteriori* LSC method , we refer to [32,17,33]. The complete set of substituting rules is not recalled here, but concisely, the new updating process for sub-cell value $\overline{\mathbf{v}}_m^{c_i,n+1}$ may fall into one of the following alternative:

$$i) \quad \frac{\mathrm{d}}{\mathrm{dt}}\left(|s_m^{c_i}(t)|\overline{\mathbf{v}}_m^{c_i}\right) = -\left(\mathcal{G}^l_{m+\frac{1}{2}} - \mathcal{G}^r_{m-\frac{1}{2}}\right) + |s_m^{c_i}(t)|\overline{\mathbf{B}}_m^{c_i}, \tag{62a}$$

$$ii) \quad \frac{\mathrm{d}}{\mathrm{dt}}\left(|s_m^{c_i}(t)|\overline{\mathbf{v}}_m^{c_i}\right) = -\left(\mathcal{G}^l_{m+\frac{1}{2}} - \widehat{\mathbf{G}}^{c_i}_{m-\frac{1}{2}}\right) + |s_m^{c_i}(t)|\overline{\mathbf{B}}_m^{c_i}, \tag{62b}$$

$$iii) \quad \frac{\mathrm{d}}{\mathrm{dt}}\left(|s_m^{c_i}(t)|\overline{\mathbf{v}}_m^{c_i}\right) = -\left(\widehat{\mathbf{G}}^{c_i}_{m+\frac{1}{2}} - \mathcal{G}^r_{m-\frac{1}{2}}\right) + |s_m^{c_i}(t)|\overline{\mathbf{B}}_m^{c_i}. \tag{62c}$$

For any mesh element $c_i(t)$ in which such fluxes corrections have occurred, leading to the computation of updated/limited sub-mean values, a new high-order polynomial candidate solution, still denoted by $\mathbf{v}_h^{n+1}$ for the sake of simplicity, is built upon these updated sub-mean values:

$$\mathbb{P}^k(c_i^n) \ni \mathbf{v}_{c_i}^{n+1} = \pi^{-1}_{\mathscr{T}_{c_i}^{n+1}}(\overline{\mathbf{v}}_{c_i}^{n+1}),$$

and the process may go further in time after checking that this new candidate is admissible.

The whole detection-correction-projection iterative process may be conveniently summarized through the application of a stabilization/correction operator denoted as follows:

$$\begin{array}{rcl} \Lambda_h^{k,n} \ : \ \left(\mathbb{P}^k\left(\mathscr{T}_h^{e,n}\right)\right)^2 & \to & \left(\mathbb{P}^k\left(\mathscr{T}_h^{e,n}\right)\right)^2, \\ \mathbf{v}_h^n & \mapsto & \Lambda_h^{k,n}(\mathbf{v}_h^n), \end{array} \tag{63}$$

where the resulting broken polynomial $\Lambda_h^{k,n}(\mathbf{v}_h^n)$ satisfies all the admissibility criteria, see §3.7. Embedding such a stabilization operator into a fully discrete version of (45a), with for instance a third order SSP-RK method, would simply gives:

$$\begin{aligned} \mathbf{v}_h^{n,(1)} &= \Lambda_h^{k,n,(1)}\Big(\mathbf{v}_h^n - \Delta t^n \mathcal{A}_h(\mathbf{v}_h^n)\Big), \\ \mathbf{v}_h^{n,(2)} &= \Lambda_h^{k,n,(2)}\Big(\frac{1}{4}(3\mathbf{v}_h^n + \mathbf{v}_h^{n,(1)}) - \frac{1}{4}\Delta t^n \mathcal{A}_h(\mathbf{v}_h^{n,(1)})\Big), \\ \mathbf{v}_h^{n+1} &= \Lambda_h^{k,n+1}\Big(\frac{1}{3}(\mathbf{v}_h^n + 2\mathbf{v}_h^{n,(2)}) - \frac{2}{3}\Delta t^n \mathcal{A}_h(\mathbf{v}_h^{n,(2)})\Big). \end{aligned} \tag{64}$$

3.10 Properties of the DG-ALE formulation with a posteriori LSC

In this section, we show that the resulting global fully discrete DG-ALE scheme with *a posteriori* LSC is globally well-balanced for motionless steady-states, satisfies the DGCL and may enjoy some local conservation property. Furthermore, as the *a posteriori* LSC method is based on a first-order FV correction, the designed algorithm is positivity-preserving by construction, see [32,17].

Well-balancing for motionless steady-states

Let begin with the well-balanced property. The following results concern the formulation (45) for the wave-obstacle problem but similar arguments may of course also be developed for the wave-piston problem. Motionless steady-states for problem (104) are trivially defined as follows:

$$\mathbf{v}(\cdot,t) = \mathbf{v}^{\mathrm{c}} = \begin{pmatrix} \eta^{\mathrm{c}} \\ 0 \end{pmatrix}, \quad \underline{q}^{\mathrm{i}}(t) = 0, \quad \varkappa_{\pm}(t) = X_0^{\pm}, \quad \forall t \geq 0. \tag{65}$$

We highlight that proving that the global semi-discrete formulation (45) preserves such steady-states is equivalent to prove that the DG-ALE scheme (45a) is well-balanced on $\mathcal{E}(t) = \mathcal{E}^-(t) \cup \mathcal{E}^+(t)$, which again reduces to ensure the property on $\mathcal{E}^-(t)$ and $\mathcal{E}^+(t)$ separately. Indeed, it is straightforward to observe that at steady-states, (45b)-(46) lead to

$$\frac{\mathrm{d}}{\mathrm{dt}}\underline{q}^{\mathrm{i}}(t) = 0, \qquad v_{\mathrm{g}|\chi_\pm}(t) = 0, \qquad \eta^i_{\chi_\pm} = \eta^{\mathrm{c}},$$

so that the coupling with the obstacle actually does not disturb the flow steady-state, thanks to the discontinuous nature of the approximation. Hence, we have the following result for the first-order in time fully discrete formulation:

Proposition 3 *The discrete formulation (45) with possible occurrence of local corrected lowest-order fluxes in one of the three possible formulations (62a)-(62b)-(62c), together with a first-order Euler time-marching algorithm, preserves the motionless steady-states (65), provided that the integrals of (45a) are exactly computed (at motionless steady-states). Specifically, for all $n \geq 0$,*

$$\left(\eta_h^n = \eta^c \text{ and } q_h^n = 0\right) \implies \left(\eta_h^{n+1} = \eta^c \text{ and } q_h^{n+1} = 0\right).$$

Proof At steady-states, for any given t and any mesh element $c(t)$, we have

$$\partial_x \mathbf{F}(\mathbf{v}_{c(t)}, b_{c(t)}) = \mathbf{B}(\mathbf{v}_{c(t)}, b'_{c(t)}). \tag{66}$$

Furthermore, both $\mathbf{F}(\mathbf{v}_h, b_h)$ and $\mathbf{B}(\mathbf{v}_h, b'_h)$ belong to $\left(\mathbb{P}^k(\mathscr{T}_h^e(t))\right)^2$ so that we have:

$$\mathbf{F}_h := p^k_{\mathscr{T}_h^e(t)}(\mathbf{F}(\mathbf{v}_h, b_h)) = \mathbf{F}(\mathbf{v}_h, b_h), \tag{67}$$

$$\mathbf{B}_h := p^k_{\mathscr{T}_h^e(t)}(\mathbf{B}(\mathbf{v}_h, b'_h)) = \mathbf{B}(\mathbf{v}_h, b'_h). \tag{68}$$

We also emphasize that it is equivalent to prove the property for the formulation (52) on the sub-partitions or for the formulation (45a) on $\mathscr{T}_h^{e,n}$. We choose to work with (52) to show that the scheme is well-balanced even at the sub-cell level, and we drop the superscript e in the remainder of this proof for the sake of simplicity:

$$\begin{aligned} &\forall c^n \in \mathscr{T}_h^{e,n}, \quad \forall m \in [\![1, \ldots, k+1]\!], \quad \overline{\eta}_m^{c,n} = \eta^c, \quad \overline{q}_m^{c,n} = 0 \\ &\qquad \implies \quad \forall c^{n+1} \in \mathscr{T}_h^{e,n+1}, \quad \forall m \in [\![1, \ldots, k+1]\!], \quad \overline{\eta}_m^{c,n+1} = \eta^c, \quad \overline{q}_m^{c,n+1} = 0. \end{aligned} \tag{69}$$

As stated in §3.9, investigating the various possibilities for the definition of the interface fluxes implies to investigate the "uncorrected" situation (52) (corresponding to high-order DG reconstructed fluxes at all sub-cells interfaces) plus three "corrected" situations enumerated in (62a)-(62b)-(62c) (and corresponding to the occurrence of modified lowest-order FV fluxes at (some of) the sub-cells interfaces). As (62b) and (62c) boil down to the same situation with a permutation of left and right fluxes, we have, for any given value $m \in [\![1, \ldots, k+1]\!]$, to distinguish three different situations:

case 1 - admissible sub-cell: $s_{m-1}^{c_i}$, $s_m^{c_i}$ and $s_{m+1}^{c_i}$ are all admissible. The sub-cell mean value $\overline{\mathbf{v}}_m^{c_i,n+1}$ is then one obtained through the uncorrected DG scheme. Equivalently, the local time-update formula with reconstructed fluxes writes

$$|s_m^{c_i,n+1}|\,\overline{\mathbf{v}}_m^{c_i,n+1} = |s_m^{c_i,n}|\,\overline{\mathbf{v}}_m^{c_i,n} - \Delta t^n\left(\widehat{\mathbf{G}}^{c_i}_{m+\frac{1}{2}} - \widehat{\mathbf{G}}^{c_i}_{m-\frac{1}{2}}\right) + \Delta t^n |s_m^{c_i,n}|\,\overline{\mathbf{B}}_m^{c_i}. \tag{70}$$

where $\widehat{\mathbf{G}}^{c_i}_{m+\frac{1}{2}}$ and $\widehat{\mathbf{G}}^{c_i}_{m-\frac{1}{2}}$ are defined in (53). We observe that at steady-state:

$$\eta^+_{i\pm\frac{1}{2}} = \eta^-_{i\pm\frac{1}{2}} = \eta^c, \qquad q^+_{i\pm\frac{1}{2}} = q^-_{i\pm\frac{1}{2}} = 0, \qquad \text{and} \qquad b^+_{i\pm\frac{1}{2}} = b^-_{i\pm\frac{1}{2}},$$

and therefore,

$$\mathbf{F}^\star_{i\pm\frac{1}{2}} = \begin{pmatrix} 0 \\ \frac{1}{2}\mathrm{g}\eta^c\left(\eta^c - 2b_{i\pm\frac{1}{2}}\right) \end{pmatrix} = \mathbf{F}\left(\mathbf{v}_{c_i|x_{i\pm\frac{1}{2}}}, b_{c_i|x_{i\pm\frac{1}{2}}}\right), \tag{71}$$

and,

$$\mathbf{v}^{\star}_{i\pm\frac{1}{2}} = \begin{pmatrix} \eta^c \\ 0 \end{pmatrix} = \mathbf{v}_{c_i|x_{i\pm\frac{1}{2}}},$$

resulting in

$$\mathbf{G}^{\star}_{i\pm\frac{1}{2}} = \mathbf{F}\Big(\mathbf{v}_{c_i|x_{i\pm\frac{1}{2}}}, b_{c_i|x_{i\pm\frac{1}{2}}}\Big) - v_{\mathrm{g}_{|i\pm\frac{1}{2}}}\mathbf{v}_{c_i|x_{i\pm\frac{1}{2}}}. \tag{72}$$

Using (67), we also have:

$$\mathbf{G}_{c_i|x_{i\pm\frac{1}{2}}} = \mathbf{F}\Big(\mathbf{v}_{c_i|x_{i\pm\frac{1}{2}}}, b_{c_i|x_{i\pm\frac{1}{2}}}\Big) - v_{\mathrm{g}_{|i\pm\frac{1}{2}}}\mathbf{v}_{c_i|x_{i\pm\frac{1}{2}}}, \tag{73}$$

thus, using the definition (53) of $\widehat{\mathbf{G}}^{c_i}_{m\pm\frac{1}{2}}$, we obtain:

$$\widehat{\mathbf{G}}^{c_i}_{m\pm\frac{1}{2}} = \mathbf{G}_{c_i|\widetilde{x}_{m\pm\frac{1}{2}}} = \mathbf{F}\Big(\mathbf{v}_{c_i|\widetilde{x}_{m\pm\frac{1}{2}}}, b_{c_i|\widetilde{x}_{m\pm\frac{1}{2}}}\Big) - v_{\mathrm{g}_{|i\pm\frac{1}{2}}}\mathbf{v}_{c_i|\widetilde{x}_{m\pm\frac{1}{2}}}, \tag{74}$$

allowing to compute the difference:

$$\widehat{\mathbf{G}}^{c_i}_{m+\frac{1}{2}} - \widehat{\mathbf{G}}^{c_i}_{m-\frac{1}{2}} = \int_{s^{c_i}_m} \partial_x \mathbf{F}(\mathbf{v}_{c_i}, b_{c_i})\,\mathrm{d}x - (v_{\mathrm{g}_{|m+\frac{1}{2}}} - v_{\mathrm{g}_{|m-\frac{1}{2}}})\mathbf{v}^c. \tag{75}$$

Additionally, updating in time the frame's interfaces with a first-order Euler scheme leads to:

$$x^{n+1} = x^n + \Delta t^n v^n_{\mathrm{g}},$$

so that the geometric term may be simplified as follows:

$$(v_{\mathrm{g}_{|m+\frac{1}{2}}} - v_{\mathrm{g}_{|m-\frac{1}{2}}})\,\mathbf{v}^c = \frac{\widetilde{x}^{n+1}_{m+\frac{1}{2}} - \widetilde{x}^{n+1}_{m-\frac{1}{2}} - (\widetilde{x}^{n}_{m+\frac{1}{2}} - \widetilde{x}^{n}_{m-\frac{1}{2}})}{\Delta t^n}\mathbf{v}^c = \frac{|s^{c_i,n+1}_m| - |s^{c_i,n}_m|}{\Delta t^n}\mathbf{v}^c.$$

Finally, (70) writes:

$$\begin{aligned}|s^{c_i,n+1}_m|\,\overline{\mathbf{v}}^{c_i,n+1}_m = |s^{c_i,n}_m|\,\mathbf{v}^c - \Delta t^n \left(\int_{s^{c_i,n}_m} \partial_x \mathbf{F}(\mathbf{v}^n_{c_i}, b_{c_i}) - \mathbf{B}(\mathbf{v}^n_{c_i}, \partial_x b_{c_i})\,\mathrm{d}x\right)\\ + |s^{c_i,n+1}_m|\,\mathbf{v}^c - |s^{c_i,n}_m|\,\mathbf{v}^c,\end{aligned}$$

and using (66), we obtain:

$$\overline{\mathbf{v}}^{c_i,n+1}_m = \mathbf{v}^c = \overline{\mathbf{v}}^{c_i,n}_m. \tag{76}$$

case 2 - neighbor of a non-admissible sub-cell: $s^{c_i}_m$, $s^{c_i}_{m-1}$ are admissible but $s^{c_i}_{m+1}$ is non-admissible (the symmetric situation of $s^{c_i}_m$, $s^{c_i}_{m+1}$ are admissible but $s^{c_i}_{m-1}$ is non-admissible may be treated in a similar way). The corresponding time-update formula is :

$$|s^{c_i,n+1}_m|\,\overline{\mathbf{v}}^{c_i,n+1}_m = |s^{c_i,n}_m|\,\overline{\mathbf{v}}^{c_i,n}_m - \Delta t^n\big(\mathcal{G}^{c_i,l}_{m+\frac{1}{2}} - \widehat{\mathbf{G}}^{c_i}_{m-\frac{1}{2}}\big) + \Delta t^n |s^{c_i,n}_m|\,\overline{\mathbf{B}}^{c_i}_m, \tag{77}$$

with $\mathcal{G}^{c_i,l}_{m+\frac{1}{2}}$ and $\widehat{\mathbf{G}}^{c_i}_{m-\frac{1}{2}}$ defined in (56)-(58) and (53). To evaluate $\mathcal{G}^{c_i,l}_{m+\frac{1}{2}}$ at steady-state, we observe that $\overline{\eta}^+_m = \overline{\eta}^-_{m+1} = \eta^c$, leading to:

$$\mathbf{F}^{\star}\left(\overline{\mathbf{v}}^+_m, \overline{\mathbf{v}}^-_{m+1}, \overline{b}^+_m, \overline{b}^+_m\right) = \frac{1}{2}\begin{pmatrix} 0 \\ \mathrm{g}\eta^c\left(\eta^c - 2\overline{b}^+_m\right)\end{pmatrix},$$

and

$$\mathcal{F}^{c_i,l}_{m+\frac{1}{2}} = \mathbf{F}\Big(\mathbf{v}_{c_i|\widetilde{x}_{m+\frac{1}{2}}}, b_{c_i|\widetilde{x}_{m+\frac{1}{2}}}\Big). \tag{78}$$

As we also have

$$\mathbf{v}^{\star,l}_{m+\frac{1}{2}} = \mathbf{v}^{\star}\left(\overline{\mathbf{v}}^+_m, \overline{\mathbf{v}}^-_{m+1}, \overline{b}^+_m, \overline{b}^+_m\right) = \mathbf{v}_{c_i|\widetilde{x}_{m+\frac{1}{2}}},$$

we obtain

$$\mathcal{G}^{c_i,l}_{m+\frac{1}{2}} = \mathbf{F}\Big(\mathbf{v}_{c_i|\widetilde{x}_{m+\frac{1}{2}}}, b_{c_i|\widetilde{x}_{m+\frac{1}{2}}}\Big) - v_{g_{|m+\frac{1}{2}}}\mathbf{v}_{c_i|\widetilde{x}_{m+\frac{1}{2}}}.$$

The computation of $\widehat{\mathbf{G}}^{c_i}_{m-\frac{1}{2}}$ is performed as in **case 1**, leading to (74) and we may evaluate the difference as follows:

$$\mathcal{G}^{c_i,l}_{m+\frac{1}{2}} - \widehat{\mathbf{G}}^{c_i}_{m-\frac{1}{2}} = \int_{s^{c_i}_m} \partial_x \mathbf{F}(\mathbf{v}_{c_i}, b_{c_i})\,\mathrm{d}x - (v_{g_{|m+\frac{1}{2}}} - v_{g_{|m-\frac{1}{2}}})\,\mathbf{v}^c, \tag{79}$$

so that,

$$\overline{\mathbf{v}}^{c_i,n+1}_m = \mathbf{v}^c = \overline{\mathbf{v}}^{c_i,n}_m.$$

case 3 - corrected sub-cell: $s^{c_i}_m$ is non-admissible. The time-update formula is:

$$|s^{c_i,n+1}_m|\,\overline{\mathbf{v}}^{c_i,n+1}_m = |s^{c_i,n}_m|\,\overline{\mathbf{v}}^{c_i,n}_m - \Delta t^n\big(\mathcal{G}^{c_i,l}_{m+\frac{1}{2}} - \mathcal{G}^{c_i,r}_{m-\frac{1}{2}}\big) + \Delta t^n |s^{c_i,n}_m|\,\overline{\mathbf{B}}^{c_i}_m. \tag{80}$$

with $\mathcal{G}^{c_i,l}_{m+\frac{1}{2}}$ and $\mathcal{G}^{c_i,r}_{m-\frac{1}{2}}$ defined in (58). Reproducing the computation steps as in **case 2**, we obtain:

$$\mathcal{G}^{c_i,l}_{m+\frac{1}{2}} = \mathbf{F}\Big(\mathbf{v}_{c_i|\widetilde{x}_{m+\frac{1}{2}}}, b_{c_i|\widetilde{x}_{m+\frac{1}{2}}}\Big) - v_{g_{|m+\frac{1}{2}}}\mathbf{v}_{c_i|\widetilde{x}_{m+\frac{1}{2}}}, \tag{81}$$

$$\mathcal{G}^{c_i,r}_{m-\frac{1}{2}} = \mathbf{F}\Big(\mathbf{v}_{c_i|\widetilde{x}_{m-\frac{1}{2}}}, b_{c_i|\widetilde{x}_{m-\frac{1}{2}}}\Big) - v_{g_{|m-\frac{1}{2}}}\mathbf{v}_{c_i|\widetilde{x}_{m-\frac{1}{2}}}, \tag{82}$$

and

$$\mathcal{G}^{c_i,l}_{m+\frac{1}{2}} - \mathcal{G}^{c_i,r}_{m-\frac{1}{2}} = \int_{s^{c_i}_m} \partial_x \mathbf{F}(v_{c_i}, b_{c_i})\,\mathrm{d}x - (v_{g_{|m+\frac{1}{2}}} - v_{g_{|m-\frac{1}{2}}})\,\mathbf{v}^c, \tag{83}$$

so that,

$$\overline{\mathbf{v}}^{c_i,n+1}_m = \mathbf{v}^c = \overline{\mathbf{v}}^{c_i,n}_m.$$

Remark 14 This well-balanced property can be extended to any higher order accuracy SSP-RK time discretization as those methods can be expressed as a convex combination of first-order Euler schemes.

Remark 15 Such a property is also provable for the wave-piston problem.

Discrete Geometric Conservation Law (DGCL)

In simulations of free-surface flows involving free moving boundaries, it is important to ensure that the proposed numerical scheme in ALE description exactly preserves uniform flows. Such preservation property is called Geometric Conservation Law in the literature and simply states that the motion of the mesh do not disturb uniform flow configurations. Hence, considering $\Omega_t = \mathcal{E}(t)$ (no piston or obstacle) and $b = 0$, we inject a uniform state $\mathbf{v}_h(\cdot,t) = (\eta^c, q^c)$ into (45a) (or equivalently (37a)), together with

$$\varphi_h(x,t) := \mathbb{1}^{c_i}(x,t) = \begin{cases} 1 & \text{if} \quad x \in c_i(t) \\ 0 & \text{if} \quad x \notin c_i(t) \end{cases},$$

to obtain:

$$\mathbf{v}^c \frac{\mathrm{d}}{\mathrm{d}t}\int_{c_i(t)} \mathrm{d}x = -\big[\!\big[\mathbf{F}(\mathbf{v}^c, 0) - v_g \mathbf{v}^c\big]\!\big]_{\partial c_i(t)} = \mathbf{v}^c\,\big[\!\big[v_g\big]\!\big]_{\partial c_i(t)},$$

and thus the GCL reduces to the following (automatically satisfied) property:

$$\frac{\mathrm{d}\,|c_i(t)|}{\mathrm{d}t} = \big[\!\big[v_g\big]\!\big]_{\partial c_i(t)}. \tag{84}$$

At the fully discrete level, we show that a fully discrete formulation, relying on an high-order SSP Runge-Kutta time discretization, satisfies the DGCL.

Proposition 4 *The DG-ALE semi-discrete scheme (45a), together with SSP-RK time-marching algorithm and the embedded stabilization operator with possible occurrence of corrected lowest-order fluxes in one of the following formulations (62a)-(62b)-(62c), preserves the DGCL. Specifically, assuming $b = 0$, we have, for any discrete time t^n:*

$$(\mathbf{v}^n_h = \mathbf{v}^c) \implies \big(\mathbf{v}^{n+1}_h = \mathbf{v}^c\big).$$

Proof Under the assumption $\mathbf{v}_h^n = \mathbf{v}^c$, we have $\mathbf{F}(\mathbf{v}_h, b_h) \in \left(\mathbb{P}^k(\mathscr{T}_h^{e,n})\right)^2$, and we observe that the following identity holds:

$$\mathbf{F}_h^n := p_{\mathscr{T}_h^{e,n}}^k(\mathbf{F}(\mathbf{v}_h^n, b_h)) = \mathbf{F}(\mathbf{v}_h^n, b_h). \tag{85}$$

As in the proof of Proposition 3, it is equivalent to show that the property holds at the sub-cell level, using formulation (52). Let us emphasize that Proposition 4 holds for any SSP-RK time discretization. The demonstration will be here specified for the third-order SSP-RK case. Let denote by $|s_m^{c_i,(1)}|$, $|s_m^{c_i,(2)}|$, and $|s_m^{c_i,n+1}|$ the length of the sub-cell $s_m^{c_i}$ at the three different time stages (and whenever the RK stage dependency has to be specified, we apply the superscripts $(.)^{(1)}$, $(.)^{(2)}$ and $(.)^{n+1}$ to the concerned quantities). The 3^{rd} order SSP-RK discretization reads as follows:

$$\begin{cases} |s_m^{c_i,(1)}|\mathbf{v}_m^{c_i,(1)} = |s_m^{c_i,n}|\mathbf{v}_m^{c_i,n} + \Delta t^n \mathcal{R}_m^{c_i,n}, \\ \\ |s_m^{c_i,(2)}|\mathbf{v}_m^{c_i,(2)} = \dfrac{3|s_m^{c_i,n}|\mathbf{v}_m^{c_i,n} + |s_m^{c_i,(1)}|\mathbf{v}_m^{c_i,(1)}}{4} + \dfrac{\Delta t^n}{4}\mathcal{R}_m^{c_i,(1)}, \\ \\ |s_m^{c_i,n+1}|\mathbf{v}_m^{c_i,n+1} = \dfrac{|s_m^{c_i,n}|\mathbf{v}_m^{c_i,n} + 2|s_m^{c_i,(2)}|\mathbf{v}_m^{c_i,(2)}}{3} + \dfrac{2\Delta t^n}{3}\mathcal{R}_m^{c_i,(2)}. \end{cases} \tag{86}$$

We have, for any given value $m \in [\![1, \dots, k+1]\!]$, to distinguish three different cases:
case 1 - admissible sub-cell: $s_{m-1}^{c_i}$, $s_m^{c_i}$ and $s_{m+1}^{c_i}$ are all admissible. The residual $\mathcal{R}_m^{c_i,(j)}$ is:

$$\mathcal{R}_m^{c_i,(j)} = -\left(\widehat{\mathbf{G}}_{m+\frac{1}{2}}^{c_i,(j)} - \widehat{\mathbf{G}}_{m-\frac{1}{2}}^{c_i,(j)}\right), \tag{87}$$

As we assume $\mathbf{v}_h^n = \mathbf{v}^c$, using (85), we get :

$$\widehat{\mathbf{G}}_{m\pm\frac{1}{2}}^{c_i,n} = \mathbf{G}_{c_i|\widetilde{x}_{m\pm\frac{1}{2}}}^n = \mathbf{F}\left(\mathbf{v}^c, 0\right) - v_{\mathrm{g}_{|m\pm\frac{1}{2}}}^n \mathbf{v}^c,$$

so that

$$\widehat{\mathbf{G}}_{m+\frac{1}{2}}^{c_i,n} - \widehat{\mathbf{G}}_{m-\frac{1}{2}}^{c_i,n} = (v_{\mathrm{g}_{|m+\frac{1}{2}}}^n - v_{\mathrm{g}_{|m-\frac{1}{2}}}^n)\mathbf{v}^c.$$

Using a similar order SSP-RK time update for the grid velocity, we obtain:

$$\begin{aligned} |s_m^{c_i,(1)}|\mathbf{v}_m^{c_i,(1)} &= |s_m^{c_i,n}|\mathbf{v}^c + \Delta t^n \left(\frac{\widetilde{x}_{m+\frac{1}{2}}^{(1)} - \widetilde{x}_{m+\frac{1}{2}}^n - \widetilde{x}_{m-\frac{1}{2}}^{(1)} + \widetilde{x}_{m-\frac{1}{2}}^n}{\Delta t^n}\right)\mathbf{v}^c \\ &= |s_m^{c_i,n}|\mathbf{v}^c + |s_m^{c_i,(1)}|\mathbf{v}^c - |s_m^{c_i,n}|\mathbf{v}^c, \\ &= |s_m^{c_i,(1)}|\mathbf{v}^c, \end{aligned}$$

and therefore:

$$\mathbf{v}_m^{c_i,(1)} = \mathbf{v}^c.$$

In a similar way, we show that $\mathbf{v}_m^{c_i,(2)} = \mathbf{v}^c$ and $\mathbf{v}_m^{c_i,n+1} = \mathbf{v}^c$, leading to the desired conclusion.

case 2 - corrected sub-cell: $s_m^{c_i}$ is non-admissible. The residual $\mathcal{R}_m^{c_i,(j)}$ is:

$$\mathcal{R}_m^{c_i,(j)} = -\left(\mathcal{G}_{m+\frac{1}{2}}^{l,c_i,(j)} - \mathcal{G}_{m-\frac{1}{2}}^{r,c_i,(j)}\right), \tag{88}$$

and one can show that we have:

$$\mathcal{G}_{m+\frac{1}{2}}^{l,c_i,n} = \mathbf{F}\left(\mathbf{v}^c, 0\right) - v_{\mathrm{g}_{|m+\frac{1}{2}}}^n \mathbf{v}^c, \quad \text{and} \quad \mathcal{G}_{m-\frac{1}{2}}^{l,c_i,n} = \mathbf{F}\left(\mathbf{v}^c, 0\right) - v_{\mathrm{g}_{|m-\frac{1}{2}}}^n \mathbf{v}^c,$$

leading to

$$\mathcal{G}_{m+\frac{1}{2}}^{l,c_i,n} - \mathcal{G}_{m-\frac{1}{2}}^{r,c_i,n} = (v_{\mathrm{g}_{|m+\frac{1}{2}}}^n - v_{\mathrm{g}_{|m-\frac{1}{2}}}^n)\mathbf{v}^c,$$

and therefore

$$\mathbf{v}_m^{c_i,n+1} = \mathbf{v}^c.$$

case 3 - neighbor of a non-admissible sub-cell: $s_m^{c_i}$, $s_{m-1}^{c_i}$ are admissible but $s_{m+1}^{c_i}$ is non-admissible (the symmetric situation of $s_m^{c_i}$, $s_{m+1}^{c_i}$ are admissible but $s_{m-1}^{c_i}$ is non-admissible may be treated in a similar way). The residual $\mathcal{R}_m^{c_i,(j)}$ in a mixed DG/FV context is:

$$\mathcal{R}_m^{c_i,(j)} = -\left(\widehat{\mathbf{G}}_{m+\frac{1}{2}}^{c_i,(j)} - \mathcal{G}_{m-\frac{1}{2}}^{r,c_i,(j)}\right). \tag{89}$$

As in the two previous situations, we have:

$$\begin{aligned}\widehat{\mathbf{G}}_{m+\frac{1}{2}}^{c_i,n} &= \mathbf{F}\left(\mathbf{v}^c, 0\right) - v_{\mathrm{g}_{|m+\frac{1}{2}}}^n \mathbf{v}^c,\\ \mathcal{G}_{m-\frac{1}{2}}^{r,c_i,,n} &= \mathbf{F}\left(\mathbf{v}^c, 0\right) - v_{\mathrm{g}_{|m-\frac{1}{2}}}^n \mathbf{v}^c,\end{aligned}$$

leading to

$$\widehat{\mathbf{G}}_{m+\frac{1}{2}}^{c_i,n} - \mathcal{G}_{m-\frac{1}{2}}^{r,c_i,n} = (v_{\mathrm{g}_{|m+\frac{1}{2}}}^n - v_{\mathrm{g}_{|m-\frac{1}{2}}}^n)\mathbf{v}^c,$$

so that,

$$\mathbf{v}_m^{c_i,n+1} = \mathbf{v}^c.$$

Lagangian flow: constant cell mass

Finally, we investigate that, given the proper grid velocity (43), our DG-ALE scheme does reach a pure Lagrangian regime, as each cell will prove to have a constant mass during the calculation.

Proposition 5 *Given (43) as grid velocity, and assuming a globally polynomial topography $b \in \mathbb{P}^k(\Omega_t)$, the semi-discrete DG-ALE formulation (37) ensures that each cell has a constant mass through the fluid flow:*

$$\forall c(t) \in \mathscr{T}_h^e(t), \quad \frac{\mathrm{d}}{\mathrm{dt}} \int_{c(t)} H_{c(t)}(\cdot,t)\, \mathrm{d}x = 0. \tag{90}$$

Proof For any $c_i(t)$ belonging to $\mathscr{T}_h^e(t)$, setting $\psi = 1$ in the first equation of the equivalent formulation (50) gives:

$$\begin{aligned}\frac{\mathrm{d}}{\mathrm{dt}} \int_{c_i(t)} \eta_{c_i(t)}\, \mathrm{d}x &:= \frac{\mathrm{d}}{\mathrm{dt}} \int_{c_i(t)} H_{c_i(t)}\, \mathrm{d}x + \frac{\mathrm{d}}{\mathrm{dt}} \int_{c_i(t)} b_{c_i(t)}\, \mathrm{d}x\\ &= -[q^\star - v_{\mathrm{g}}(\cdot,t)\eta^\star]_{x_{i-\frac{1}{2}}(t)}^{x_{i+\frac{1}{2}}(t)}.\end{aligned} \tag{91}$$

Then, noting that $b_{c_i(t)} = b$ as the topography is assumed to be globally polynomial, one observes:

$$\begin{aligned}\frac{\mathrm{d}}{\mathrm{dt}} \int_{c_i(t)} b_{c_i(t)}\, \mathrm{d}x &= \int_{c_i(0)} \frac{\mathrm{d}}{\mathrm{dt}}\Big(b\big(x(X,t)\big) \cdot \mathcal{J}(X,t)\Big)\, \mathrm{d}X\\ &= \int_{c_i(t)} \underbrace{\partial_t b(x)}_{=0} + v_{\mathrm{g}}(x,t)\partial_x b(x) + b(x)\partial_x v_{\mathrm{g}}(x,t)\, \mathrm{d}x\\ &= [b\, v_{\mathrm{g}}(\cdot,t)]_{x_{i-\frac{1}{2}}(t)}^{x_{i+\frac{1}{2}}(t)}.\end{aligned} \tag{92}$$

Since $\eta^\star = H^\star + b$, it directly follows that:

$$\forall c(t) \in \mathscr{T}_h^e(t), \quad \frac{\mathrm{d}}{\mathrm{dt}} \int_{c(t)} H_{c(t)}(\cdot,t)\, \mathrm{d}x = -\Big[q^\star - v_{\mathrm{g}}(\cdot,t)(\eta^\star - b)\Big]_{x_{i-\frac{1}{2}}(t)}^{x_{i+\frac{1}{2}}(t)}.$$

The use of (43) as frame's velocity gives the desired result. Let us mention that this result further holds at the discrete level.

4 Numerical validations

In this section, we provide several numerical assessments of the DG-ALE discrete formulations (37) and (45). In the following test-cases, if not stated differently, we display sub-mean values instead of point-wise values. Also, in test-cases associated with (45), we consider surface obstacles with elliptic shapes, and the reader is referred to C for explicit formulae.
The remainder of this section is split into three parts: (i) some general validations of the DG-ALE formulation for the NSW equations (pure fluid model), (ii) two test-cases dedicated to the assessment of the wave-piston model (37), (iii) four test-cases associated with the wave-obstacle (45).

4.1 DG-ALE formulation for NSW equations

To begin with, we investigate the ability of the stabilized DG-ALE formulation to deal with the propagation of an initial discontinuity within a pseudo-Lagrangian description, and to ensure the well-balancing property while enforcing some arbitrary grid's motion.

4.1.1 Dam-break with a pseudo-Lagrangian grid's motion

This first test-case is dedicated to the numerical assessment of the DG-ALE implementation with *a posteriori* LSC method for the pure NSW fluid model and we consider a classical dam-break problem. Hence we only consider the formulation (37a), considering that $\Omega_t = \mathcal{E}(t)$, and enforcing homogeneous Neumann boundary conditions on $\partial\Omega_t$. We initially define $\mathcal{E}(0) = [0, 1]$, together with the following initial data:

$$\eta_0(x) := \begin{cases} 1 & \text{if} \quad x \leq 0.5, \\ 0.5 & \text{elsewhere,} \end{cases}, \qquad q_0 := 0,$$

and we set $T_{\max} = 0.075\,s$, $n_{\text{el}} = 50$, $k = 3$. For this test-case, the frame's velocity is defined in a *pseudo-Lagrangian* using the definition (43) of $v_{\text{g}}(t)$. We show on Fig. 6-left a snapshot of the free-surface at $t = 0.075\,s$ and we highlight the *corrected* and *uncorrected* sub-cells on the right. This illustrates that the correction is activated only in a very thin area in the vicinity of the discontinuity, preventing the occurrence of spurious oscillations. Finally, to demonstrate how this *a posteriori* LSC method with ALE moving grid scales going to very high-orders of accuracy and very coarse meshes, we run the same test with $k = 9$ and a 10 mesh elements. The corresponding numerical result is shown on Fig. 7. One can see how the shock has been resolved in only one sub-cell, while still ensuring a non-oscillatory behavior. This result further illustrates the high capability of this *a posteriori* LSC method with ALE moving grid to retain the precise subcell resolution of discontinuous Galerkin schemes, allowing the use of very coarse meshes, along with being able to avoid the appearance of spurious oscillations or any unfortunate crash of the code.

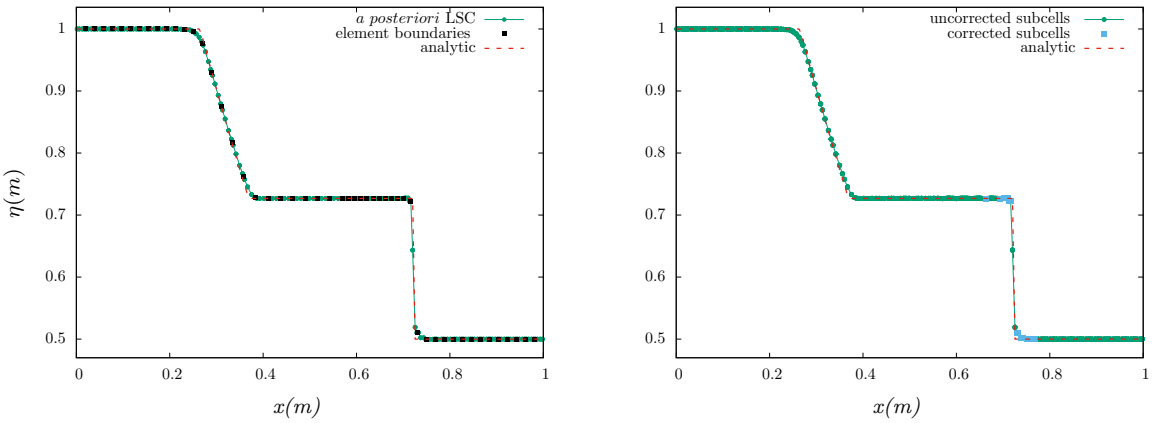

Fig. 6: Test 4.1.1 - Dam-break with a pseudo-Lagrangian grid's motion - Free-surface elevation computed at $t = 0.075\,s$, for $k = 3$ and $n_{\text{el}} = 50$ (left). The corrected and uncorrected sub-cells are displayed on the right.

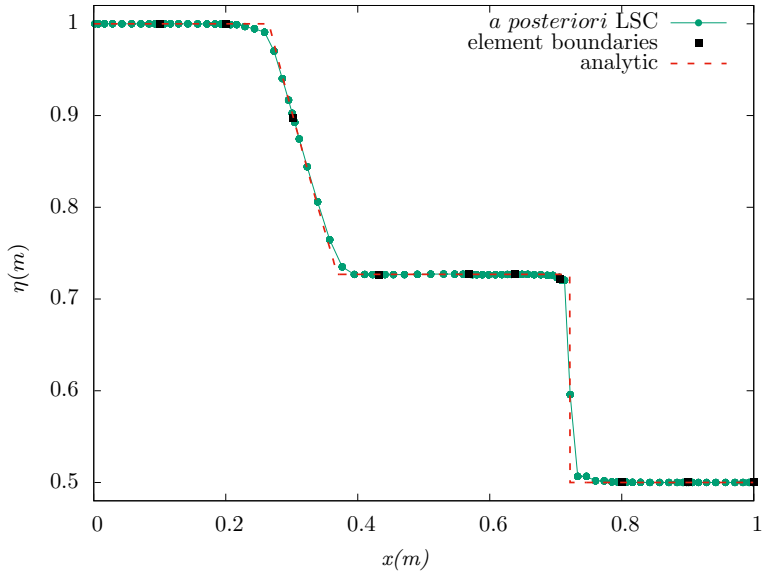

Fig. 7: Test 4.1.1 - Dam-break with a pseudo-Lagrangian grid's motion - Free-surface elevation computed at $t = 0.075\,s$, for $k = 9$ and $n_{\text{el}} = 10$.

4.1.2 Well-balancing with an arbitrary grid's motion

Next, we aim at assessing the motionless steady-states preservation property. This property has already been studied for the DG method with *a posteriori* LSC method in [17] and, as a consequence, we only consider the validation the property with a moving grid. We initially consider $\Omega_0 = \mathcal{E}(0) := [0, 1]$ (pure fluid model) with a topography defined as follows:

$$b(x) := \begin{cases} A\left(\sin\left(\dfrac{(x - x_1)\cdot\pi}{75}\right)\right)^2 & \text{if} \quad x_1 \leq x \leq x_2, \\ 0 & \text{elsewhere,} \end{cases} \tag{93}$$

with $A = 4.75$, $x_1 = 0.125\,m$ and $x_2 = 0.875\,m$, and the initial data is defined as:

$$\eta_0 := 10, \qquad q_0 := 0,$$

see Fig. 8. We set $k = 3$, $n_{\text{el}} = 50$ and, for this particular test only, the grid's velocity is arbitrary and uniformly set to $v_{\text{g}} := 0.01\ \text{m}\cdot\text{s}^{-1}$. We perform 10^6 time iterations, allowing the computation to march in time until $T_{\max} = 50\,s$, and we confirm that the initial data is preserved up to the machine accuracy, while Ω_0 is translated of $0.5\,m$ rightward. A similar behavior is of course reported for alternate combinations of k, n_{el} and v_{g}.

4.2 Wave - piston interactions

In the two following test-cases, we focus on the model (4)-(5)-(6) and the corresponding discrete formulation (37).

4.2.1 Prescribed motion

Considering a constrained motion for the piston in $\mathcal{I}(t)$, one can neglect the Newton's law (6) for the motion of the piston, and directly enforce $\dot{\chi}$, only considering the influence of the piston on the water and mimicking, for instance, the motion of a wave-paddle. The computational domain is defined as $\Omega_t = [-100, 100]$, the free-surface is initially set to $\eta^0 = H_0 = 10\,m$ and the initial discharge is set to 0. The right boundary is assumed to coincide with the initial location of the piston. The fluid motion is then generated by enforcing some periodic horizontal displacement of the piston, as follows:

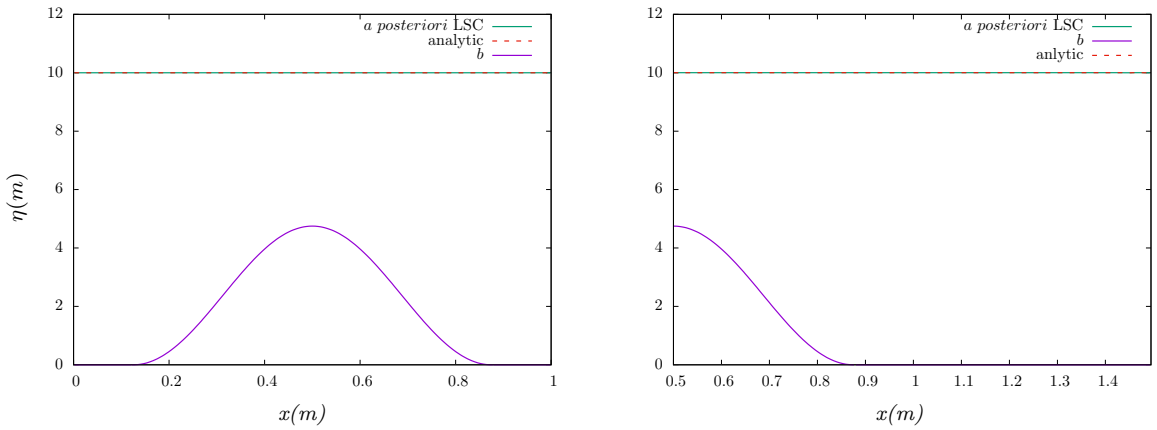

Fig. 8: Test 4.1.2 - Well-balancing with an arbitrary grid's motion - Free-surface elevation at $t_0 = 0\,s$ (left), and $T_{\max} = 50\,s$ (right).

$$\chi(t) := 90 + 10\cos\left(\frac{2\pi t}{40}\right),$$

and we enforce some homogeneous Neumann condition at the left boundary of the domain, allowing the incoming waves to (sufficiently for our purpose) leave the domain. We set $k = 3$, $n_{\text{el}} = 100$ and we compute the time-evolution of the coupled system up to $T_{\max} = 50\,s$. The water elevation and wall position at several times in the range $[0\,s,\ 50\,s]$ on the interval $[-100, 100]$ are shown on Fig. 9.

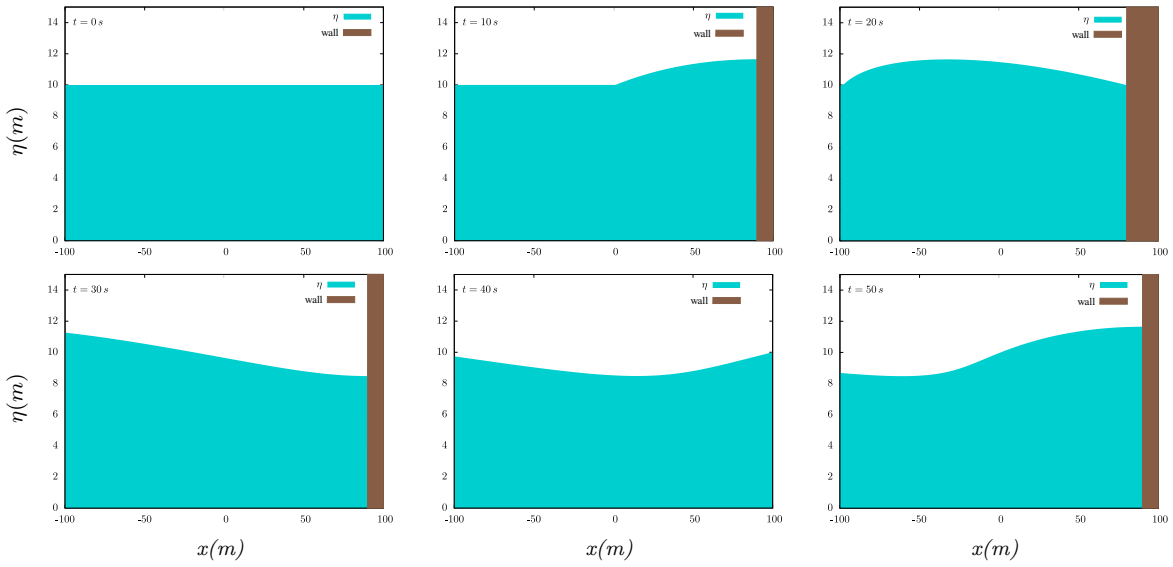

Fig. 9: Test 4.2.1 - Wave-piston model in prescribed motion - Free-surface obtained at several times in the range $[0\,s,\ 50\,s]$, with $k = 3$ and $n_{\text{el}} = 100$.

4.2.2 A single wave interacting with a lateral piston

In this test-case, we investigate the evolution of a system made of a lateral piston which moves under the respective influence of the pressure applied by the water and of a spring force that tends to bring it back to its initial position. We consider the computational domain $\Omega_t = [0, 110]$, the mean water-depth is $H_0 = 5\,m$ and we set $(\chi, \dot{\chi})_{|t=0} := (100, 0)$, *i.e.* the piston is initially located at $X^0 = 100\,m$ with $\dot{X}^0 = 0$

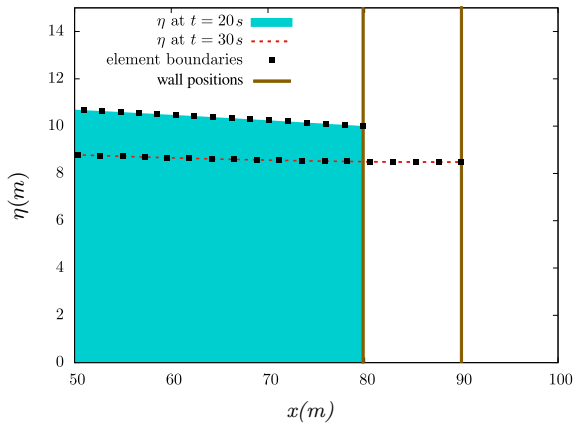

Fig. 10: Test 4.2.1 - Wave-piston model in prescribed motion - Free-surface elevation: comparison between numerical solutions at $t = 20\,s$ and $t = 30\,s$, with $k = 3$, $n_{\text{el}} = 100$.

and $\mathcal{E}(0) = [0, 100]$. The piston's mass is set to $m = 100\,\text{kg}$ and the spring stiffness to $k = 10^4\text{N/m}$, such that the whole system water-piston is initially in equilibrium and the spring is initially partly compressed. Although solitary waves are not classical solutions of the NSW equations, we observe that for small amplitudes, solitary wave solutions of more elaborated dispersive models may be propagated without too much distortion over limited distances, before becoming singular. Hence, starting from the system in equilibrium and assuming that $b = 0$, we consider a rightward propagating single wave initially defined as follows:

$$\eta^0(x) := H_0 + A_w \,\text{sech}^2\left(\gamma\,(x - x_c)\right), \qquad q^0(x) := \sqrt{\frac{g}{H_0}}(\eta^0(x) - H_0)\eta^0(x), \tag{94}$$

with $A_w = 0.35\,m$, $\gamma := \sqrt{\dfrac{3A}{4H_0}}$ and $x_c = 65\,m$, see Fig 11, and we investigate its interactions with the piston. We set $k = 3$, $n_{\text{el}} = 100$ and we compute the time-evolution of the coupled system up to $T_{\max} = 60\,s$, with an homogeneous Neumann condition at the left boundary. We show on Fig. 12 some snapshots of the free-surface elevation at several discrete time between $t = 2.2\,s$ and $t = 60\,s$. We observe the wave run-up and run-down on the wall, before being fully reflected, propagating leftward and being evacuated from the computational domain. As expected, we observe that the additional hydrodynamic pressure applied on the piston during the wave run-up compress the spring, pushing the piston rightward, before letting it coming back to its equilibrium location after the wave's reflection.

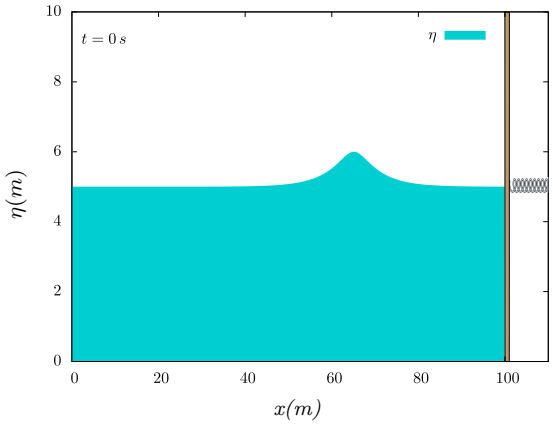

Fig. 11: Test 4.2.2 - A single wave interacting with a lateral piston - Free-surface elevation at initial time with $k = 3$, $n_{\text{el}} = 100$.

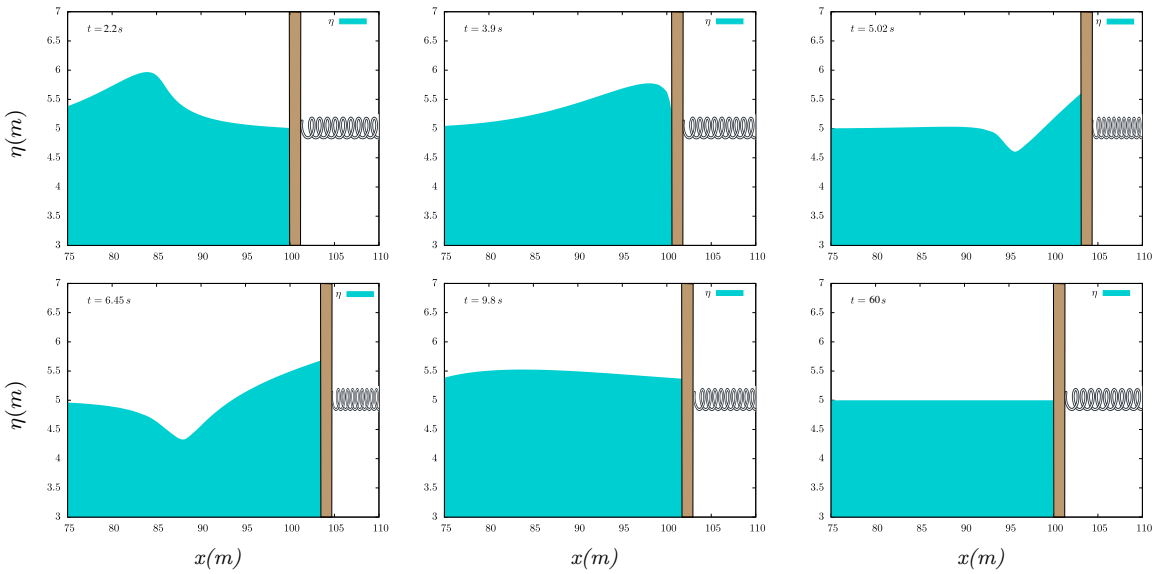

Fig. 12: Test 4.2.2 - A single wave interacting with a lateral piston - Free-surface obtained at several times in the range $[2.2\,s,\ 60\,s]$, with $k = 3$ and $n_{\text{el}} = 100$. Zoom on water/piston interaction zone.

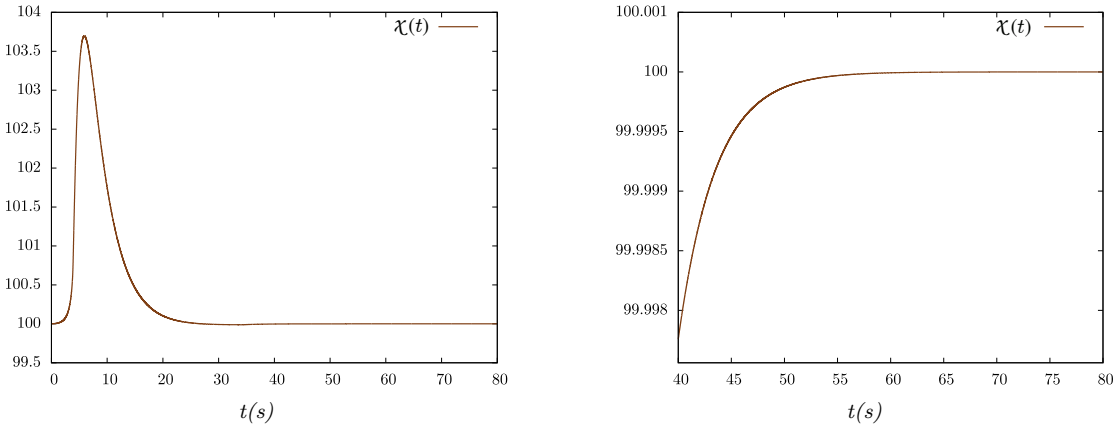

Fig. 13: Test 4.2.2 - A single wave interacting with a lateral piston - Variation of the horizontal coordinate of the water/piston contact point $\chi(t)$, for k = 3, $n_{\text{el}} = 100$ in the range [0 s, 80 s].

To complete the picture, we also assess that, given the proper grid velocity (43), the DG-ALE method does reach a pure Lagrangian behavior, as each cell will prove to have a constant mass during the calculation. To this end, we replace the left Neumann condition by a non-penetration condition mimicking the presence of a solid wall and, for each mesh element, we define the cell mass as well as the relative cell mass variation:

$$m_{\text{f}}^i(t) := \int_{c_i(t)} H(\cdot, t)\,\mathrm{d}x, \qquad E_{m_{\text{f}}}^i := \left| \frac{m_{\text{f}}^i(t) - m_{\text{f}}^i(0)}{m_{\text{f}}^i(0)} \right|. \tag{95}$$

Finally, we compute the time evolution up to $t = 100\,s$ of the total relative mass variation as follows:

$$E_{m_{\text{f}}} = \sum_{i=1}^{n_{\text{el}}} E_{m_{\text{f}}}^i. \tag{96}$$

As expected, the cell masses are preserved up to machine precision, see Fig. 14. This result further reasserts that the presented scheme preserves the DGCL, as if it was not the case, the cell volume

computed through the updated grid points position and the one computed as the ratio between the initial cell mass and the updated water height average value could be different. This is actually how the DGCL preservation property is addressed in the pure Lagrangian community.

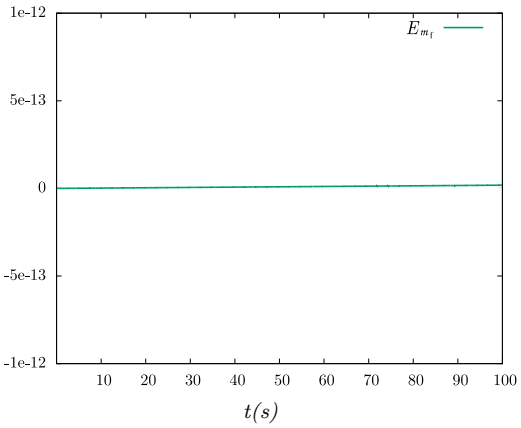

Fig. 14: Test 4.2.2 - A single wave interacting with a lateral piston - total relative error, for k = 3, $n_{\text{el}} = 100$ in the range [0 s, 100 s].

4.3 Waves interactions with a surface obstacle

4.3.1 Well-balancing property

In this test-case, we aim at assessing the motionless steady-states preservation property, with a partly immersed surface obstacle. We consider $\Omega_t := [-50, 200]$, with a topography profile defined as follows

$$b(x) := \begin{cases} A\left(\sin\left(\dfrac{(x-x_1)\cdot\pi}{75}\right)\right)^2 & \text{if} \quad x_1 \le x \le x_2, \\ \dfrac{1}{\beta}(x-x_3) & \text{if} \quad x \ge x_3, \\ 0 & \text{elsewhere,} \end{cases} \tag{97}$$

where $A = 1.5\,m$, $\beta = 11$, $x_1 = 12.5\,m$, $x_2 = 87.5\,m$ and $x_3 = 90\,m$ and we place a surface obstacle with an elliptic shape at $(x_G, z_G) := (50, H_0 + 2.5)$, with $H_0 = 5\,m$. The elliptic obstacle is defined with respective horizontal and vertical radii $R_1 = 10\,m$ and $R_2 = 5\,m$, and its center of mass is located at $(x_{\text{G}}, z_{\text{G}})$ (see C for the detailed definition of the obstacle). In Figure 23, the partly immersed surface obstacle is depicted, with the same dimensions that will be used in the following test cases. We highlight that, for a better visualization of the numerical results, different scales for x and η axes may be used in the remaining figures, see for instance Figure 15, leading to visually misleading proportions.

For this particular test case, the initial data in $\mathcal{E}^0$ is defined as

$$\eta^0(x) := \max\left(5, b(x)\right), \qquad q^0 := 0,$$

while in the interior domain $\mathcal{I}^0$ we set:

$$\eta^i(\cdot, 0) := \mathrm{p}^k_{\mathscr{T}_h^{i,0}}(\eta_{\text{lid}}), \qquad q^i(0) := 0.$$

We evolve this initial configuration up to $T_{\max} = 50\,s$, with $k = 3$, $n^e_{\text{el}} = 50$ and $n^i_{\text{el}} = 10$. The free-surface elevation obtained with the DG-ALE scheme using the *a posteriori* LSC method is shown on Fig. 15. The corrected and uncorrected sub-cells are exhibited on Fig. 16, with a zoom in the vicinity of the obstacle where the *a posteriori* LSC method is active. The motionless steady-state is preserved up to the machine accuracy and this property is also satisfied using various combinations of k, n^e_{el} and n^i_{el}.

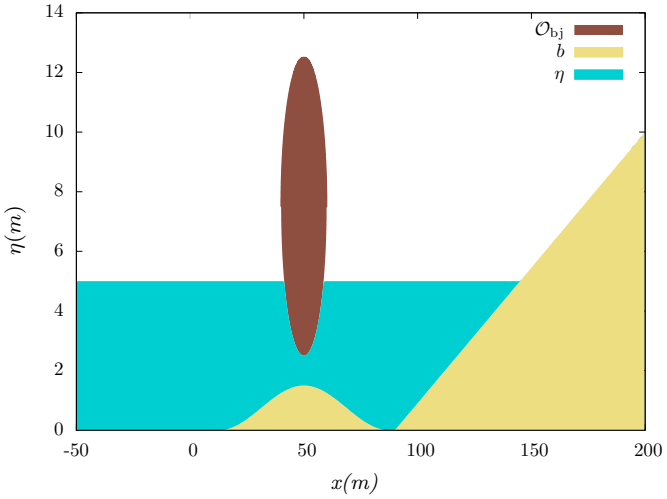

Fig. 15: Test 4.3.1 - Preservation of a motionless steady-state with a surface obstacle - Free-surface elevation at $T_{\max} = 50\,s$, with $k = 3$, $n^e_{\text{el}} = 50$, $n^i_{\text{el}} = 10$.

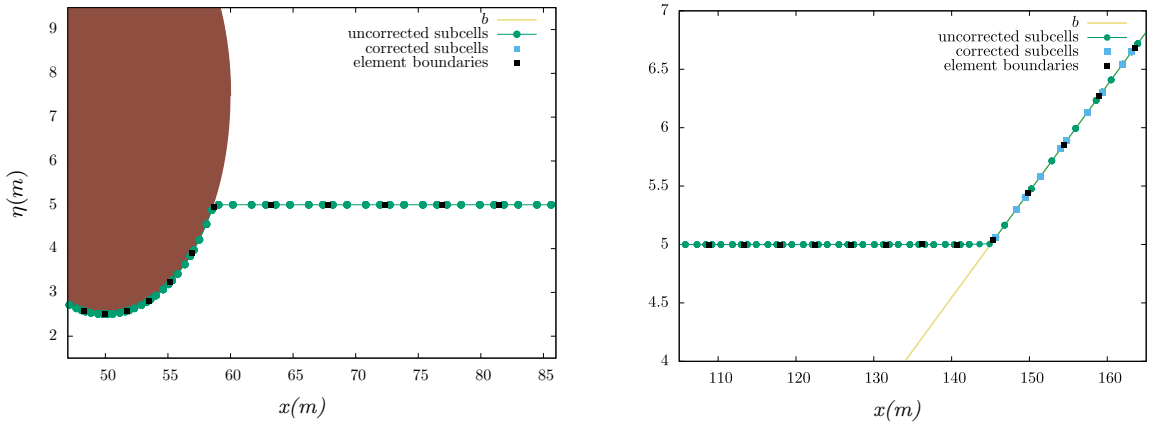

Fig. 16: Test 4.3.1 - Preservation of a motionless steady-state with a surface obstacle - Free-surface elevation at $T_{\max} = 50\,s$, with a zoom near the obstacle (left) and the shoreline (right), showing the corrected and the uncorrected sub-cells, for $k = 3$, $n^e_{\text{el}} = 50$, $n^i_{\text{el}} = 10$.

4.3.2 A single wave interacting with a surface obstacle

Next, we focus on the interactions between a single wave propagating towards a surface obstacle, over a varying topography made of a bump. We consider the computational domain $\Omega_t := [0, 100]$, with $H_0 = 5\,m$ and the topography profile is defined as follows:

$$b(x) := \begin{cases} A_b \left(\sin\left(\dfrac{(x - x_1) \cdot \pi}{75} \right) \right)^2 & \text{if} \quad x_1 \leq x \leq x_2, \\ 0 & \text{elsewhere,} \end{cases} \tag{98}$$

with $A_b = 1.5\,m$, $x_1 = 12.5\,m$ and $x_2 = 87.5\,m$. A stationary obstacle with an elliptic shape is placed over the bump, the initial data in $\mathcal{E}^0$ is defined using the single wave formula (94) with $A_w = 0.35\,m$ and $x_c = 20\,m$, and the initial data in $\mathcal{I}^0$ is defined as in the previous test. The elliptic obstacle is, as before, defined with respective horizontal and vertical radii $R_1 = 10\,m$ and $R_2 = 5\,m$, and its center of mass is located at $(x_{\text{G}}, z_{\text{G}}) = (50, H_0 + 2.5)$. We set $n^e_{\text{el}} = 50$, $n^i_{\text{el}} = 10$ and $k = 3$. Snapshots of the free-surface at various times during the propagation are shown on Fig. 17, together with the corresponding values of the discharge, and the normalized pressure beneath the obstacle. Interestingly, we observe a partial run-up, run-down and reflection on the obstacle's left side. This reflected wave goes back towards the inlet

boundary, while the transmitted wave propagates further beyond the obstacle, into the right exterior domain, finally, both reflected and transmitted wave are evacuated from the computational domain, thanks to the Neumann boundary conditions on $\partial\Omega_t$.

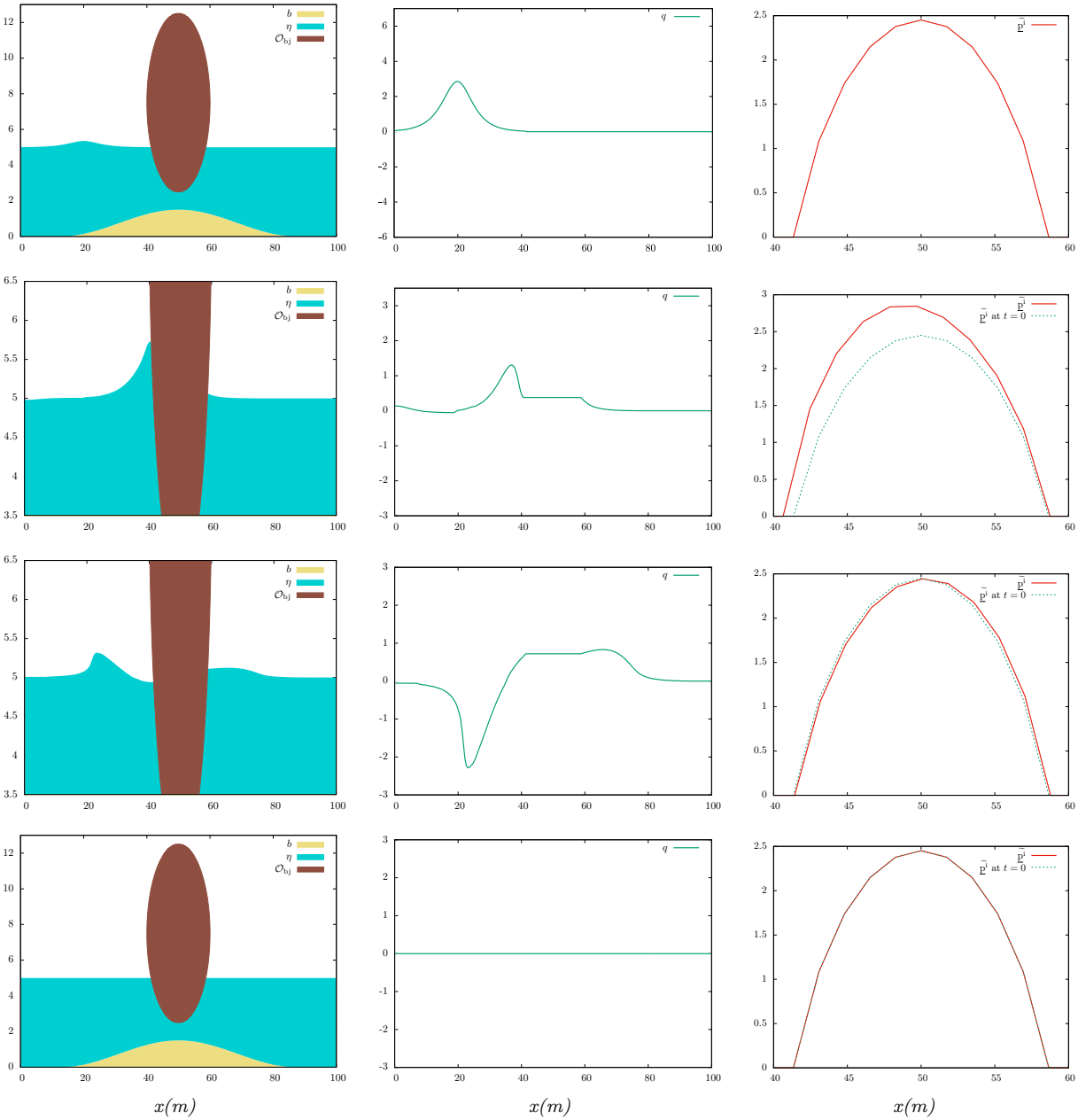

Fig. 17: Test 4.3.2 - A single wave interacting with a surfce obstacle: surface elevation η, discharge q and inner pressure $\underline{\widetilde{p}}^{\mathrm{i}} = \underline{p}^{\mathrm{i}}/\rho g$ at the underside of the obstacle for $n_{\mathrm{el}}^{e} = 50$, $n_{\mathrm{el}}^{i} = 10$ and $k = 3$.

4.3.3 A shock-wave interacting with a surface obstacle

In this test, we consider a shock-wave propagating over a flat bottom, with a surface obstacle located in the middle of the domain, in order to highlight the stabilization capabilities of the *a posteriori* LSC method in the vicinity of the obstacle and emphasize the robustness of the resulting global DG-ALE

formulation. We set $\Omega_t := [-20, 120]$, $n_{\rm el}^e = 70$, $n_{\rm el}^i = 10$ and $k = 3$. The initial data is defined as follows:

$$\eta^0(x) := \begin{cases} 6.5 & \text{if} \quad x \leq 0, \\ 5 & \text{elsewhere}, \end{cases}, \quad \eta^i(\cdot, 0) := \mathrm{p}^k_{\mathscr{T}_h^{i,0}}(\eta_{\rm lid}), \qquad q^0 := 0, \qquad q^{\rm i}(0) := 0.$$

Snapshots of the free-surface elevation at several time are shown on Fig. 18. We observe that the discontinuity, initially located in $\mathcal{E}_0^-$, propagates towards the obstacle, generating some interesting nonlinear interactions. We emphasize that this configuration simultaneously involves a shock-wave propagation and reflection, displacement of the frame through the ALE description, a partial run-up over the surface-piercing obstacle which is associated with the collision between the shock-wave and the obstacle left-side and a partial transmission of the wave beyond the obstacle with the formation of an interesting free-surface profile that looks like a rarefaction wave. This highlights the robustness of the global formulation and in particular the stabilization effect associated with the *a posteriori* LSC method . The dynamic of the free-boundaries is indeed computed in a very stable way, without any spurious oscillations or further time-step restriction. Additionally, a zoom on the free-surface discontinuity is displayed on Fig. 19, highlighting that the *a posteriori* LSC method is only activated in a very thin area in the vicinity of the propagating shock-wave.

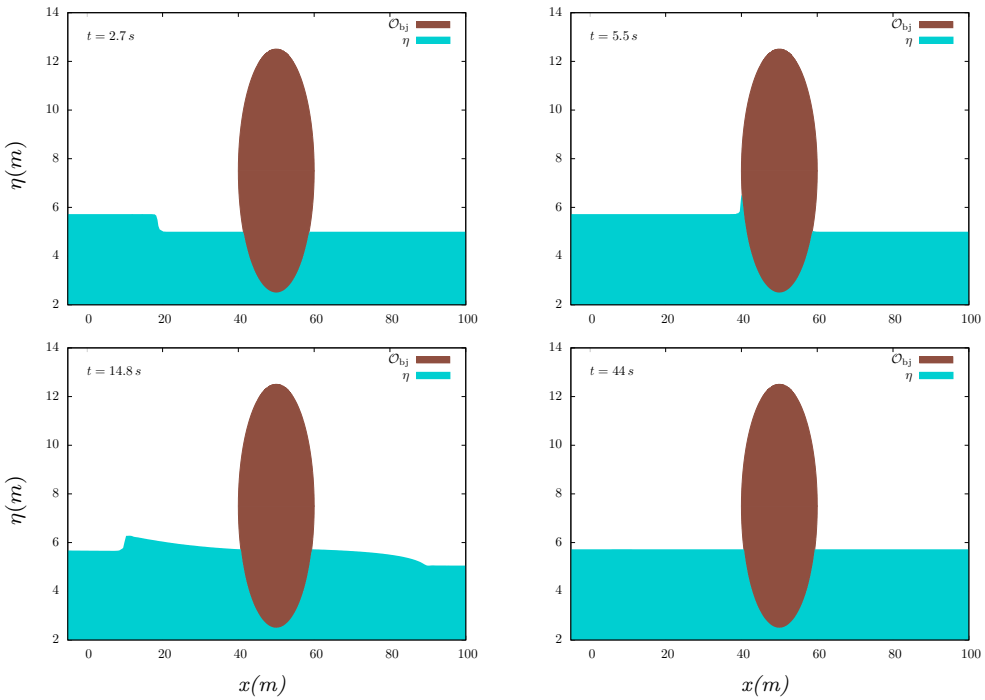

Fig. 18: Test 4.3.3 - A shock-wave interacting with a surface obstacle - Free-surface elevation computed at various times: $t = 2.7\,s$, $5.5\,s$, $14.8\,s$ and $44\,s$ with $k = 3$, $n_{\rm el}^e = 70$ and $n_{\rm el}^i = 10$.

4.3.4 Run-up of a single wave party reflected by a surface obstacle

In this last test-case, we follow the propagation and run-up of a single wave over a plane beach, with a surface obstacle placed on the way. The computational domain is set to $\Omega_t := [-200, 150]$, the topography is made of a constant depth area followed by a sloping beach of constant slope $1/11$. We set $k = 3$, $n_{\rm el}^e = 50$ and $n_{\rm el}^i = 10$. The single wave is defined as in (11) with $A_w = 0.55\,m$ and $x_c = -80\,m$. We show on Fig. 20 some snapshots of the free-surface elevation at several discrete times in the range $(0.57\,s, 300\,s)$. We observe a partial run-up and reflection of the wave on the obstacle, while the remaining part of the wave is transmitted beyond the obstacle, propagating further in $\mathcal{E}(t)$. This secondary wave subsequently reaches the shore, generating a run-up on the beach followed by a reflection. This reflected wave is itself again partially reflected by the obstacle, generating a third sequence of run-up and reflection, while the

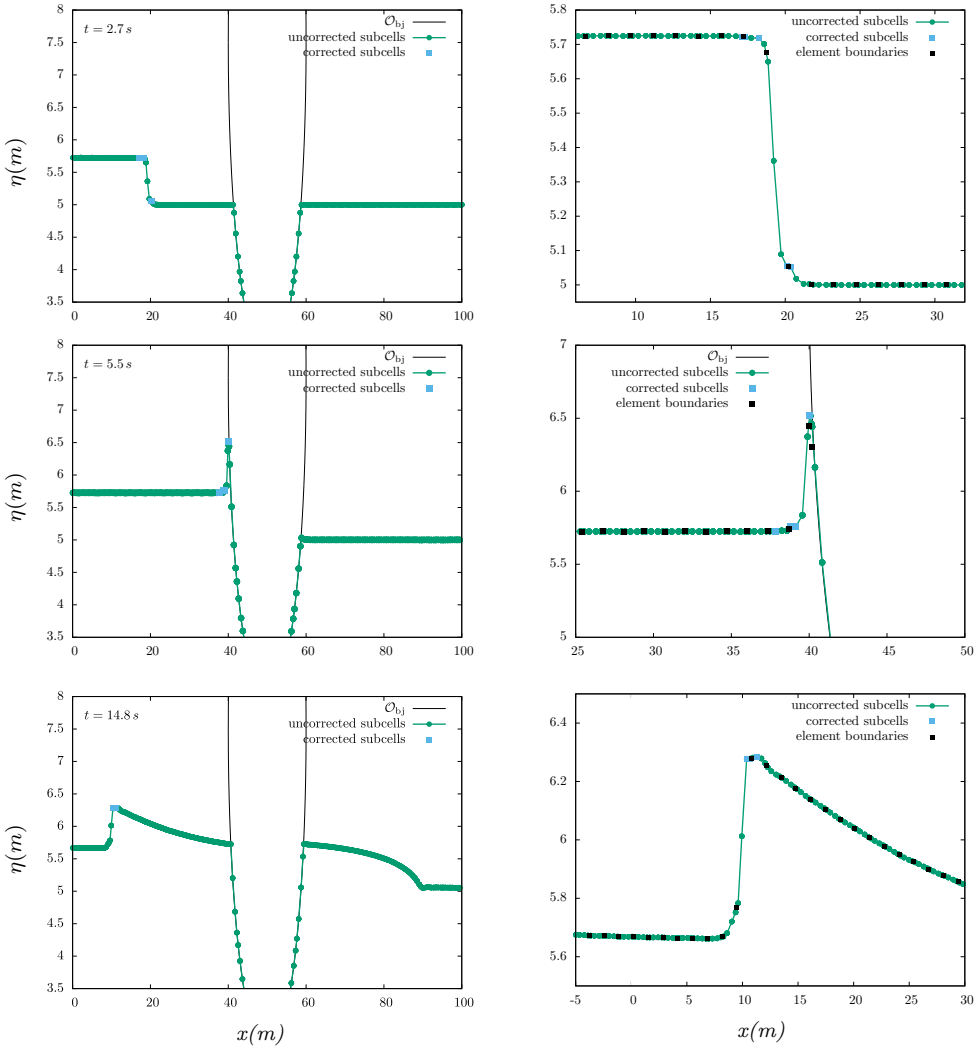

Fig. 19: Test 4.3.3 - A shock-wave interacting with a surface obstacle - Free-surface elevation computed for different values of time $t = 2.7\,s$, $5.5\,s$ and $14.8\,s$. The corrected and uncorrected sub-cells are respectively plotted with blue squares and green dots, with a zoom on the discontinuity, for $k = 3$, $n^e_{\text{el}} = 70$ and $n^i_{\text{el}} = 10$.

transmitted wave propagates back in $\mathcal{E}^-(t)$ towards the domain's left boundary. In Fig. 21, we zoom on the shoreline area, highlighting the corrected and uncorrected sub-cells which are respectively plotted with green squares and blue dots. Again, we observe that the *a posteriori* LSC method is only activated in a very thin area in the vicinity of the wet/dry front. We also display on Fig. 22 a comparison between the maximum run-up observed with and without the embedded partially immersed obstacle on place, in order to highlight the impact of the obstacle presence on the run-up amplitude.

5 Conclusion

In this paper, we introduce a novel numerical approximation algorithm allowing to compute fluid-structure interactions between a partially immersed and stationary obstacle in shallow water flows. This new discrete formulation is based on a DG-ALE global discretization for the flow model, coupled with a set of nonlinear ordinary differential equations for the resolution of the free-boundary problems associated with the time evolution of the air-fluid-structure interface, and the time evolution of the discharge beneath the obstacle. In order to allow the computation of general waves interactions, possibly involving non-smooth surface waves, we extend the *a posteriori* LSC method of [17] to the current DG-ALE description. In particular, we show that the resulting global flow discrete formulation preserves the DGCL, as well as

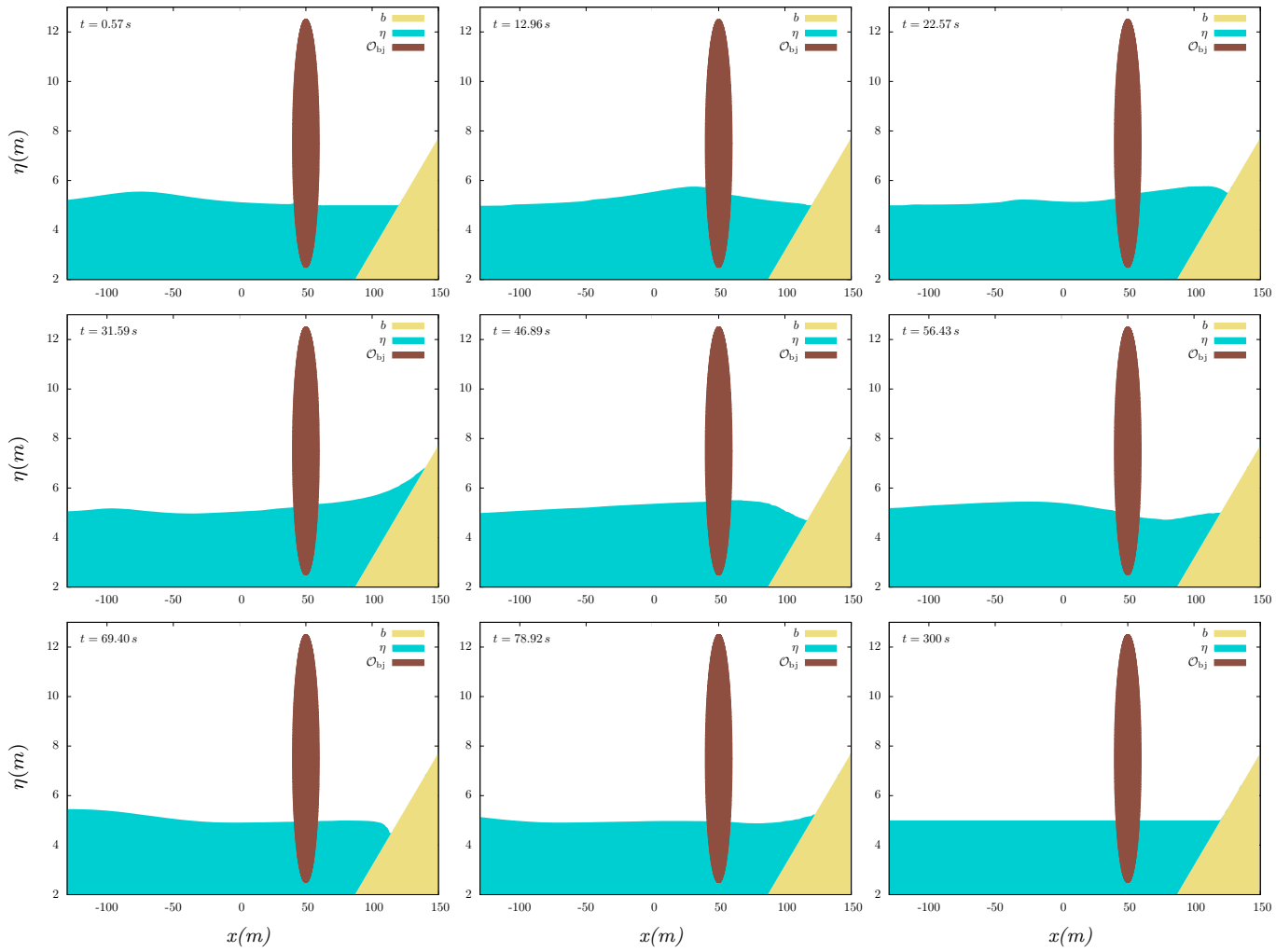

Fig. 20: Test 4.3.4 - Run-up of a single wave partly reflected by a stationary obstacle - Free-surface obtained at several times in the range $[0.57\,s,\ 300\,s]$, with $k = 3$ and $n_{\text{el}}^e = 50$, $n_{\text{el}}^i = 10$.

the well-balancing property for motionless steady-states, for any order of approximation in space. The resulting numerical strategy combines the high accuracy of DG approximations, with a robust stabilization process which ensures the positivity of the water height at the sub-cell level, as well as preventing from the occurrence of spurious oscillations in the vicinity of discontinuities, discontinuities of the gradient and extrema.
More general configurations involving moving floating objects are investigated in an upcoming and closely related work.

A Coupled PDE-ODE model for the flow with a surface obstacle

Let $\underline{\mathrm{p}}^{\mathrm{i}}(x,t)$ be the pressure of the water at the underside of the obstacle. The pressure field in the whole domain is assumed to be hydrostatic:

$$\mathrm{p}(x,z,t) := \begin{cases} \mathrm{p}_{\mathrm{atm}} - \rho \mathrm{g}(z - \eta^e(x,t)) & \text{in} \quad \mathcal{E}(t), \\ \underline{\mathrm{p}}^{\mathrm{i}}(x,t) - \rho \mathrm{g}(z - \eta^i(x,t)) & \text{in} \quad \mathcal{I}(t), \end{cases} \tag{99}$$

where ρ is the density of the water and $\mathrm{p}_{\mathrm{atm}}$ the atmospheric pressure. Thus, the general shallow water model with a surface obstacle reads as follows:

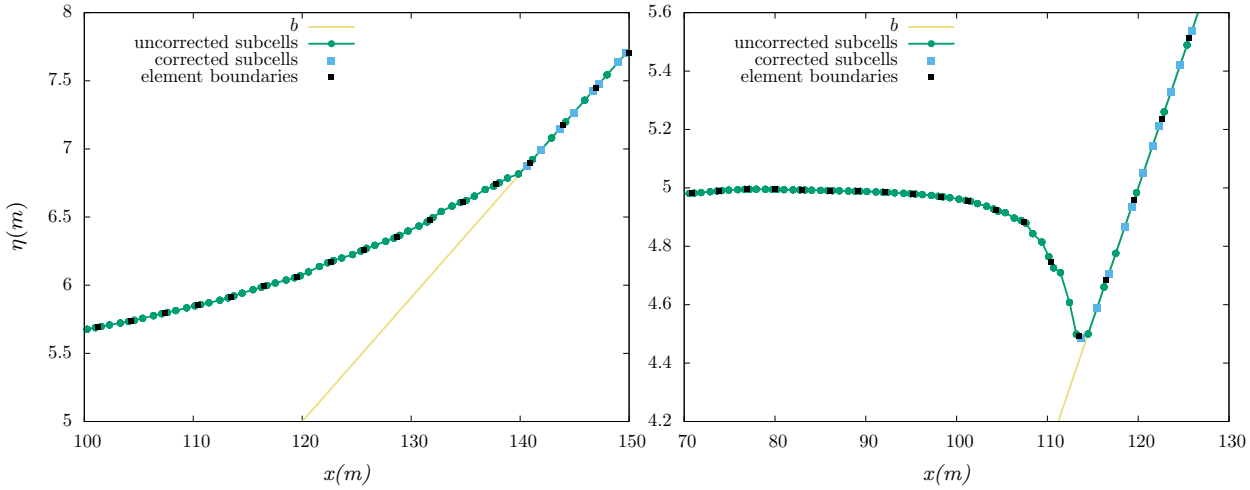

Fig. 21: Test 4.3.4 - Run-up of a single wave partially reflected by a stationary obstacle - Zoom on the shoreline showing the free-surface at $t = 31.59\,s$ (left) and $t = 69.40\,s$ (right), with corrected and uncorrected sub-cells respectively plotted with blue squares and green dots, for $k = 3$ and $n^e_{\text{el}} = 50$, $n^i_{\text{el}} = 10$.

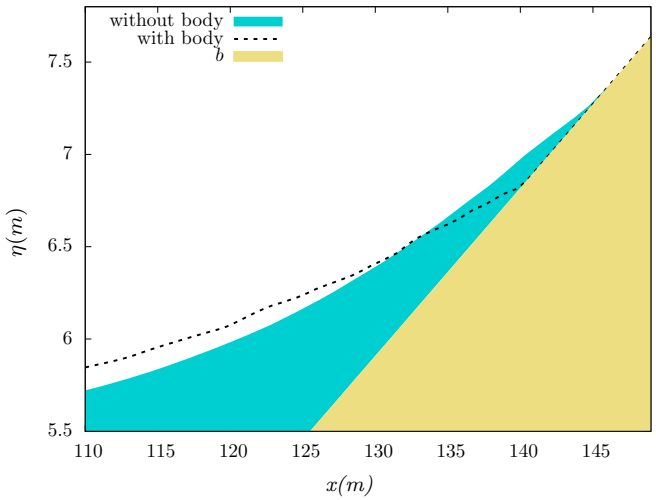

Fig. 22: Test 4.3.4 - Run-up of a single wave partially reflected by a stationary obstacle - Snapshot of the free-surface corresponding to the maximum run-up observed with the embedded partly immersed obstacle (in dashed-line) and without the obstacle (in blue).

$$
\begin{cases}
\mathcal{E}(t) = \left]-\infty,\, \chi_{\leftarrow}(t)\right[\cup \left]\chi_{+}(t),\, +\infty\right[\quad \text{and} \quad \mathcal{I}(t) = \left]\chi_{\leftarrow}(t), \chi_{+}(t)\right[, & \text{(100a)} \\
\left.\begin{aligned} &\partial_t \eta^e + \partial_x q^e = 0, \\ &\partial_t q^e + \partial_x \left(u^e q^e + \frac{1}{2} \mathrm{g} \eta^e (\eta^e - 2b) \right) = -\mathrm{g} \eta^e b', \end{aligned}\right\} \quad \text{in} \quad \mathcal{E}(t) & \text{(100b)} \\
\left.\begin{aligned} &\partial_t \eta^i + \partial_x q^i = 0, \\ &\partial_t q^i + \partial_x \left(u^i q^i + \frac{1}{2} \mathrm{g} (H^i)^2 \right) = -\mathrm{g} H^i b' - \tfrac{1}{\rho} H^i \partial_x \underline{\mathrm{p}}^{\mathrm{i}}, \end{aligned}\right\} \quad \text{in} \quad \mathcal{I}(t) & \text{(100c)} \\
\eta^e = \eta^i, \quad q^e = q^i \quad \text{and} \quad \underline{\mathrm{p}}^{\mathrm{i}} = \mathrm{p}_{\mathrm{atm}} \quad \text{at} \quad \chi_{\pm}(t) & \text{(100d)}
\end{cases}
$$

The obstacle being stationary, η^i locally coincides with the parameterization of the obstacle's boundary and does not explicitly depend on time (though it implicitly depends on time as $\mathcal{I}(t)$ does):

$$\eta^i(x,t) := \eta_{\rm lid}(x) \quad \text{on} \quad \mathcal{I}(t) \subset \mathcal{I}_{\rm lid}, \tag{101}$$

where $\eta_{\rm lid}$ is a given function defined on $\mathcal{I}_{\rm lid}$, which is the open interval where the parameterization of the obstacle's underside is defined, see Fig. 3.4. Thus, the continuity equation in $\mathcal{I}(t)$ in (100) yields $\partial_x q^i = 0$ and therefore $q^i(x,t) = \underline{q}^{\rm i}(t)$. Injecting this into the momentum equation for the interior sub-domain in (100), we obtain:

$$\frac{1}{H_i}\frac{{\rm d}\,\underline{q}^{\rm i}}{{\rm dt}} + \partial_x\Big(\frac{1}{2}\big(\frac{\underline{q}^{\rm i}}{H^i}\big)^2 + {\rm g}H^i\Big) = -{\rm g}b' - \frac{1}{\rho}\partial_x \underline{\rm p}^{\rm i},$$

so that $\underline{\rm p}^{\rm i}$ satisfies the following Boundary Value Problem (BVP):

$$\begin{cases} \partial_x \underline{\rm p}^{\rm i} = -\rho\left(\dfrac{1}{H_i}\dfrac{{\rm d}\,\underline{q}^{\rm i}}{{\rm dt}} + \partial_x\big(\dfrac{1}{2}\big(\dfrac{\underline{q}^{\rm i}}{H^i}\big)^2 + {\rm g}\eta^i\big)\right) & \text{in} \quad \mathcal{I}(t), \qquad (102a) \\ \underline{\rm p}^{\rm i} = {\rm p}_{\rm atm} & \text{on} \quad \mathcal{E}(t)\cap\mathcal{I}(t). \qquad (102b) \end{cases}$$

Integrating (102a) on $\mathcal{I}(t)$, we get:

$$\frac{{\rm d}\,\underline{q}^{\rm i}}{{\rm dt}} = -\Big(\int_{\mathcal{I}(t)}\frac{1}{H^i}\,{\rm d}x\Big)^{-1}\Big[\!\Big[\frac{1}{2}\Big(\frac{\underline{q}^{\rm i}}{H^i}\Big)^2 + {\rm g}\eta^i\Big]\!\Big]_{\mathcal{I}(t)}. \tag{103}$$

As a consequence, in the particular case of free-surface shallow water flows with a surface obstacle, the general model (100) may be simplified as follows:

$$\begin{cases} \mathcal{E}(t) = \,]\!-\!\infty, \varkappa_-(t)[\,\cup\,]\varkappa_+(t), +\infty[\quad \text{and} \quad \mathcal{I}(t) = \,]\varkappa_-(t), \varkappa_+(t)[, & (104a) \\ \partial_t \mathbf{v} + \partial_x \mathbf{F}(\mathbf{v}, b) = \mathbf{B}(\mathbf{v}, b') & \text{in} \quad \mathcal{E}(t), \qquad (104b) \\ \left.\begin{array}{l} \eta^i = \eta_{\rm lid}, \\ \dfrac{{\rm d}\,\underline{q}^{\rm i}}{{\rm dt}} = -\Big(\displaystyle\int_{\mathcal{I}(t)}\frac{1}{H^i}\,{\rm d}x\Big)^{-1}\Big[\!\Big[\frac{1}{2}\Big(\frac{\underline{q}^{\rm i}}{H^i}\Big)^2 + {\rm g}\eta^i\Big]\!\Big]_{\mathcal{I}(t)}, \end{array}\right\} & \text{in} \quad \mathcal{I}(t), \qquad (104c) \\ \eta^e = \eta^i \quad \text{and} \quad q^e = q^i & \text{at} \quad \varkappa_\pm(t). \qquad (104d) \end{cases}$$

B Cut-off function

The cut-off function $\varphi \in \mathcal{D}(\mathbb{R})$ used in (47) is defined as follows:

$$\forall x \in \mathbb{R}, \quad \varphi(x) := e\,\psi_e(\varepsilon_0 x),$$

where

$$\forall x \in \mathbb{R}, \quad \psi_e(x) := \phi_e(1 - |x|^2),$$

and

$$\forall t \in \mathbb{R}, \quad \phi_e(t) := \begin{cases} e^{-t^{-1}} & \text{if} \quad t > 0 \\ 0 & \text{elsewhere,} \end{cases}$$

Note that we have ${\rm supp}(\psi_e) \subset \overline{B}(0,1)$, ${\rm supp}(\varphi) \subset [-\frac{1}{\varepsilon_0}, \frac{1}{\varepsilon_0}]$ and ε_0 chosen such that we have $\varphi(x) = 1$, $\forall |x| \leq 1$.

C Definition of the elliptic obstacle

In this work, we consider a partially immersed obstacle $\mathcal{O}_{\rm bj}$, which center of mass is located at $(x_{\rm G}, z_{\rm G})$ and which boundary is denoted by $\partial\mathcal{O}_{\rm bj}$. Denoted respectively by R_1, R_2 its major and minor radii, we define $\partial\mathcal{O}_{\rm bj}$ as an ellipse, so that we have:

$$(x,y) \in \partial\mathcal{O}_{\rm bj} \iff \frac{(x-x_{\rm G})^2}{R_1^2} + \frac{(z-z_{\rm G})^2}{R_2^2} = 1.$$

The underside of the obstacle may be locally parameterized as follows:

$$\forall x \in \mathcal{I}_{\rm lid} := [x_{\rm G} - R_1, x_{\rm G} + R_1], \quad \eta_{\rm lid}(x) := z_{\rm G} - R_2\sqrt{1 - \frac{(x-x_{\rm G})^2}{R_1^2}}.$$

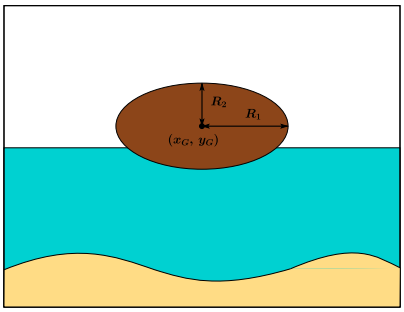

Fig. 23: Representation of the surface obstacle with $R_1 = 10$ and $R_2 = 5$.

Let e_0 denotes the elevation of the center of mass of $\mathcal{O}_{\mathrm{bj}}$ above the mean water-depth H_0 at initial time. Denoting $z_{\mathrm{G}} = H_0 + e_0$ ($e_0 = 2.5\,m$ in the test cases), we have:

$$X_0^{\pm} := x_{\mathrm{G}} \pm \sqrt{R_1^2 - \frac{R_1^2 {e_0}^2}{R_2^2}}.$$

Declarations

Data availability

Data sharing not applicable to this article as no datasets were generated or analyzed during the current study.

Conflicts of interest

The authors declare that they have no conflicts of interest in the present work.

Acknowledgement

We would like to extend our sincere appreciation to David Lannes for his invaluable support and contributions

References

1. L. Arpia and M. Ricchiuto. Well balanced residual distribution for the ALE spherical shallow water equations on moving adaptive meshes. *J. Comput. Phys.*, 405:109–173, 2019.
2. G. Beck and D. Lannes. Freely floating objects on a fluid governed by the Boussinesq equations. *Annales de l'Institut Henri Poincaré C*, 39(3):575–646, 2022.
3. S. Benzoni-Gavages and D. Serre. *Multidimensional Hyperbolic Partial Differential Equations - First-order Systems and Applications*. Oxford university Press, 2007.
4. E. Bocchi, J. He, and G. Vergara-Hermosilla. Modelling and simulation of a wave energy convertor. In *A venir*, 2020.
5. U. Bosi, A.P. Engsig-Karup, C. Eskilsson, and M. Ricchiuto. A spectral/hp element depth-integrated model for nonlinear wave–body interaction. *Comp. Meth. App. Mech. Eng.*, 348:22–249, 2019.
6. D. Bresch, D. Lannes, and G. Métivier. Waves interacting with a partially immersed obstacle in the Boussinesq regime. *Analysis and PDE*, 14(4):1085–1124, 2021.
7. Q. Chen and I. Babuska. Approximate optimal points for polynomial interpolation of real functions in an interval and in a triangle. *Comput. Methods Appl. Mech. Engrg*, 128:405–417, 1995.
8. B. Cockburn and C.-W. Shu. Runge-Kutta Discontinuous Galerkin methods for convection-dominated problems. *J. Sci. Comput.*, 16(3):173–260, 2001.
9. A.J.-C. de Saint-Venant. Théorie du mouvement non-permanent des eaux, avec application aux crues des rivières et à l'introduction des marées dans leur lit. *C.R. Acad. Sci. Paris, Section Mécanique*, 73:147–154, 1871.
10. J. Donea, A. Huerta, J.-Ph. Ponthot, and A. Rodríguez-Ferran. *Arbitrary Lagrangian–Eulerian Methods, The Encyclopedia of Computational Mechanics*, pages 413–437. Wiley, 2004.
11. A. Duran and F. Marche. Recent advances on the discontinuous Galerkin method for shallow water equations with topography source terms. *Comput. Fluids*, 101:88–104, 2014.
12. Allan P. Engsig-Karup, Jan S. Hesthaven, Harry B. Bingham, and T. Warburton. Dg-fem solution for nonlinear wave-structure interaction using Boussinesq-type equations. *Coastal Engineering*, 55:197–208, 2008.
13. E. Godlewski, M. Parisot, J. Sainte-Marie, and F. Wahl. Congested shallow water model: roof modelling in free surface flow. *ESAIM Math. Model. Numer. Anal.*, 52(5):1679 – 1707, 2018.

14. S. Gottlieb, C.-W. Shu, and Tadmor E. Strong stability preserving high order time discretization methods. *SIAM Review*, 43:89–112, 2001.
15. E. Guerrero Fernàndez, M. J. Castro Díaz, M. Dumbser, and T. Morales de Luna. An arbitrary high order well-balanced ader-dg numerical scheme for the multilayer shallow-water model with variable density. *Journal of Scientific Computing*, 90, 2022.
16. H. Guillard and C. Farhat. On the significance of the geometric conservation law for flow computations on moving meshes. *Comput. Methods Appl. Engrg*, 190:1467–1482, 2000.
17. A. Haidar, F. Marche, and F. Vilar. A posteriori finite-volume local subcell correction of high-order discontinuous Galerkin schemes for the nonlinear shallow-water equations. *J. Comput. Phys.*, 452:110902, 2022.
18. C.W. Hirt, A.A. Amsden, and J.L. Cook. An arbitrary lagrangian–eulerian computing method for all flow speed. *J. Comput. Phys.*, 135:203–216, 1997.
19. T. Iguchi and D. Lannes. Hyperbolic free boundary problems and applications to wave-structure interactions. *Indiana Univ. Math. J.*, 70:353–464, 2021.
20. M. Ioriatti and M. Dumbser. A posteriori sub-cell finite volume limiting of staggered semi-implicit discontinuous Galerkin schemes for the shallow water equations. *Applied Numerical Mathematics*, 135:443–480, 2019.
21. G. Khakimzyanov and D. Dutykh. Numerical modelling of surface water wave interaction with a moving wall. *Commun. Comput. Phys.*, 23:1289–1354, 2018.
22. A. Korobkin, S. Stukolov, , and I. Sturova. Motion of a vertical wall fixed on springs under the action of surface waves. *Journal of applied mechanics and technical physics*, 50(5):841–849, 2009.
23. D. Lannes. *The water waves problem: mathematical analysis and asymptotics*. Number 188 in Mathematical Surveys and Monographs. American Mathematical Society, 2013.
24. Q. Liang and F. Marche. Numerical resolution of well-balanced shallow water equations with complex source terms. *Advances in Water Resources*, 32(6):873 – 884, 2009.
25. I. Lomtev, R.M. Kirby, and G.E. Karniadakis. A discontinuous Galerkin ALE method for compressible viscous flows in moving domains. *J. Comput. Phys.*, 155(1):128–159, 1999.
26. P.-O. Persson, J. Peraire, and J. Bonet. Discontinuous Galerkin solution of the Navier–Stokes equations on deformable domains. *Comp. Meth. App. Mech. Eng.*, 198:1585–1595, 2009.
27. C.-W. Shu and S. Osher. Efficient implementation of Essentially Non-Oscillatory shock-capturing schemes. *J. Comput. Phys.*, 77:439–471, 1988.
28. P.D. Thomas and C.K. Lombard. Geometric conservation law and its applications to flow computations on moving grids. *AIAA Journal*, 17:1030–1037., 1979.
29. J.J.W. van de Vegt and Y. Xu. Space-time discontinuous galerkin method for nonlinear water waves. *J. Comput. Phys.*, 224:17–39, 2007.
30. J.J.W. Van der Vegt and H. Van der Ven. Space-time discontinuous Galerkin finite element method with dynamic grid motion for inviscid compressible flows. *J. Comput. Phys.*, 182:546–585, 2002.
31. C.S. Ventakasubban. A new finite element formulation for ALE (arbitrary Lagrangian Eulerian) compressible fluid mechanics. *Int. J. Engrg. Sci.*, 33:1743–1762, 1995.
32. F. Vilar. A posteriori correction of high-order discontinuous galerkin scheme through subcell finite volume formulation and flux reconstruction. *J. Comput. Phys.*, 387:245–279, 2019.
33. F. Vilar and R. Abgrall. A posteriori local subcell correction of high-order discontinuous galerkin scheme for conservation laws on two-dimensional unstructured grids. *SIAM J. Sci. Comput.*, Submitted, 2022.